NASA TECHNICAL REPORT

NASA TR R-413

NASA TR R-413

ANALYSIS OF THE INJECTION OF A HEATED TURBULENT JET INTO A CROSS FLOW

by James F. Campbell and Joseph A. Schetz

Langley Research Center
Hampton, Va. 23665

NATIONAL AERONAUTICS AND SPACE ADMINISTRATION • WASHINGTON, D. C. • DECEMBER 1973

1. Report No.	2. Government Accession No.	3. Recipient's Catalog No.
NASA TR R-413		

4. Title and Subtitle	5. Report Date
ANALYSIS OF THE INJECTION OF A HEATED TURBULENT JET INTO A CROSS FLOW	December 1973
	6. Performing Organization Code

7. Author(s)	8. Performing Organization Report No.
James F. Campbell and Joseph A. Schetz (Virginia Polytechnic Institute and State University)	L-8987
	10. Work Unit No. 160-75-17-02

9. Performing Organization Name and Address	11. Contract or Grant No.
NASA Langley Research Center Hampton, Va. 23665	
	13. Type of Report and Period Covered Technical Report

12. Sponsoring Agency Name and Address	14. Sponsoring Agency Code
National Aeronautics and Space Administration Washington, D.C. 20546	

15. Supplementary Notes The information presented herein was included in a thesis submitted by James F. Campbell, entitled "Analysis of the Injection of a Heated, Turbulent Jet into a Moving Mainstream, With Emphasis on a Thermal Discharge in a Waterway," in partial fulfillment of the requirements for the degree of Doctor of Philosophy in Aerospace Engineering, Virginia Polytechnic Institute and State University, Blacksburg, Virginia, December 1972.

16. Abstract

An investigation has been undertaken to develop a theoretical model of the incompressible jet injection process. The discharge of a turbulent jet into a cross flow was mathematically modeled by using an integral method which accounts for natural fluid mechanisms such as turbulence, entrainment, buoyancy, and heat transfer. The analytical results are supported by experimental data and demonstrate the usefulness of the theory for estimating the trajectory and flow properties of the jet for a variety of injection conditions. The capability of predicting jet flow properties, as well as two- and three-dimensional jet paths, was enhanced by obtaining the jet cross-sectional area during the solution of the conservation equations (a number of previous studies assume a specific growth for the area). Realistic estimates of temperature in the jet fluid were acquired by accounting for heat losses in the jet flow due to forced convection and to entrainment of free-stream fluid into the jet.

17. Key Words (Suggested by Author(s))	18. Distribution Statement
Fluid mechanics Thermodynamics and combustion	Unclassified – Unlimited

19. Security Classif. (of this report)	20. Security Classif. (of this page)	21. No. of Pages	22. Price*
Unclassified	Unclassified	63	Domestic, $3.50 Foreign, $6.00

*For sale by the National Technical Information Service, Springfield, Virginia 22151

CONTENTS

ANALYSIS OF THE INJECTION OF A HEATED TURBULENT JET INTO A CROSS FLOW*

By James F. Campbell and Joseph A. Schetz†
Langley Research Center

SUMMARY

An investigation has been undertaken to develop a theoretical model of the incompressible jet injection process. The discharge of a turbulent jet into a cross flow was mathematically modeled by using an integral method which accounts for natural fluid mechanisms such as turbulence, entrainment, buoyancy, and heat transfer. The analytical results are supported by experimental data and demonstrate the usefulness of the theory for estimating the trajectory and flow properties of the jet for a variety of injection conditions. The capability of predicting jet flow properties, as well as two- and three-dimensional jet paths, was enhanced by obtaining the jet cross-sectional area during the solution of the conservation equations (a number of previous studies assume a specific growth for the area). Realistic estimates of temperature in the jet fluid were acquired by accounting for heat losses in the jet flow due to forced convection and to entrainment of free-stream fluid into the jet.

INTRODUCTION

One of the more basic processes in fluid mechanics is the mixing that occurs during the interaction of two intersecting streams of fluid. A large portion of such interaction processes exists where one stream of fluid has a much smaller mass (or volume) flow than the other stream, such as the case of a plume issuing from a smoke stack or a fluid injecting into a boundary layer on a vehicle traversing the atmosphere. This class of interaction problems, categorized as fluid or jet injection processes, is usually associated with a nearby solid boundary or surface. These injection processes are complicated by the fact that in their natural state they are almost invariably turbulent.

---

*The information presented herein was included in a thesis submitted by James F. Campbell, entitled "Analysis of the Injection of a Heated, Turbulent Jet into a Moving Mainstream, With Emphasis on a Thermal Discharge in a Waterway," in partial fulfillment of the requirements for the degree of Doctor of Philosophy in Aerospace Engineering, Virginia Polytechnic Institute and State University, Blacksburg, Virginia, December 1972.

†Virginia Polytechnic Institute and State University.

Details of the jet injection process have been obtained by a number of experimenters (refs. 1 to 13) and reveal the very complex velocity and temperature fields that exist due to the interaction of the jet flow with the cross flow. Theoretical attempts (refs. 14 to 22) to model this interaction process have usually considered the injected fluid as a turbulent momentum jet having a two-dimensional path. Since a large number of physical problems are concerned with jets having three-dimensional paths, it is desirable to have a theory that is capable of calculating three-dimensional jet trajectories as well as one which allows estimates of jet flow properties to be made.

Accordingly, the present study was initiated to develop a theoretical method which accounts for the pertinent fluid-mechanic and heat-transfer aspects of heated turbulent jets discharging into a cross flow. The injection process is assumed to be incompressible where the jet flow injects into a cross flow of semi-infinite extent and to have a spatially dependent velocity field. Emphasis has been given to determining the effects of the ambient flow variables and injection conditions on the jet path and to examining how the flow properties of and heat loss from the jet vary along the path.

The general development of the theoretical model is presented in the main body of the report along with comparisons with other analytical methods and with experimental data acquired from a number of investigations. Details of the theory are contained in the appendixes.

SYMBOLS

A cross-sectional area of jet control volume

A_i area of jet orifice, $\pi d_i^2/4$

C effective jet circumference, $\sqrt{4\pi A}$

C_D drag coefficient

C_p pressure coefficient

c_p specific heat at constant pressure of jet fluid

D drag on jet flow due to blockage of free-stream flow

d effective jet diameter, $\sqrt{4A/\pi}$

d_i diameter of jet orifice

ds	differential length of jet control volume
$d\delta$	elemental area
$d\sigma$	elemental volume
E	entrained mass flow per unit length of jet
E^*	entrainment coefficient
$\vec{e}_N$	unit vector normal to elemental area $d\delta$
$\vec{e}_s,\vec{e}_n,\vec{e}_t$	unit vectors in natural coordinate system
$\vec{e}_x,\vec{e}_y,\vec{e}_z$	unit vectors in Cartesian coordinate system
F_p	pressure force
f_b	body force acting on elemental volume $d\sigma$
f_c	centrifugal force per unit volume
f_g	buoyancy force per unit volume
g	gravity acceleration constant
H	average film heat-transfer coefficient
h	width of jet control volume
J	nondimensional entrainment parameter, see equation (B2)
j	finite-difference grid point
k	thermal conductivity of jet fluid
m	mass of jet fluid in control volume
m_e	free-stream mass entrained into control volume

$N_{Fr,i}$	Froude number of jet flow at injection point, $2V_i^2 \Big/ \left[\bar{d}_i g(\rho_\infty - \rho_i)/\rho_i\right]$
$N_{Nu,d}$	Nusselt number based on effective jet diameter, Hd/k
N_{Pr}	Prandtl number
$N_{Re,d}$	Reynolds number based on effective jet diameter, see equation (47)
$N_{Re,di}$	Reynolds number of jet flow at injection point, $V_i d_i / \nu_i$
p	local static pressure around perimeter of jet cross section
$\bar{p}$	average static pressure in jet flow
p_∞	free-stream static pressure
Q	rate of heat flow from jet control volume
q	average dynamic pressure of jet flow, $\rho V^2/2$
q_∞	average dynamic pressure of free-stream flow, $\rho_\infty V_\infty^2/2$
R	radius of curvature of jet trajectory
$\vec{r}$	position vector from injection point to a point on the jet trajectory, see figure 32
S_c	effective cylindrical area of jet control volume, $\pi d \Delta s$
S_{ref}	reference area of jet control volume
s,n,t	natural coordinate system attached to jet trajectory, see figure 32
T	average temperature of jet fluid, see equation (4)
T_∞	average temperature of free-stream fluid
$\tilde{t}$	time, see equations (1) and (9)

u,w	direction cosines, $\cos \alpha$ and $\cos \beta$, respectively
V	average velocity of jet flow, see equation (4)
$\vec{V}$	velocity vector
V_e	entrainment velocity, see equation (B5)
V_{eff}	effective velocity ratio, $\left[\left(\rho_i V_i^2\right)/\left(\rho_\infty V_\infty^2\right)\right]^{1/2}$
V_∞	average free-stream velocity
x,y,z	Cartesian (inertial) coordinate system, see figure 2
y_o	point above injection surface where laminar jet flow is assumed to begin its turbulent growth
α,β,γ	inclination of jet axis with respect to X-, Y-, and Z-axis, respectively, see figure 32
Δs	infinitesimal length of jet control volume
ΔT	temperature difference, $T - T_\infty$
η	defines expression in equation (A22)
θ	angular orientation, see figure 8
Λ	defines expression in equation (A23)
μ	coefficient of viscosity
ν	kinematic viscosity
ρ	average density of jet fluid, see equation (4)
ρ_∞	average density of free-stream fluid

$\bar{\bar{\tau}}$ surface stress tensor

τ_o torsion of jet trajectory, see equation (A9)

ψ,ξ constants in expression for $N_{Nu,d}$, see equation (46)

Subscripts:

i conditions at point of jet injection

l local value of jet flow property

nom nominal

s,n,t conditions in s-, n-, and t-direction, respectively

1,2 jet flow conditions in control volume before and after entrainment

①,②,③ surfaces of jet control volume, see figure 2

∞ conditions associated with the free-stream flow

Arrow over symbol indicates vector.

REVIEW OF LITERATURE

There are a variety of problem areas in incompressible flow situations that would benefit from understanding the basic fluid injection process. In aeronautical disciplines some of these areas are boundary-layer control, jet flap technology, fuel injection, aeroacoustics, and V/STOL aerodynamics. In the environmental sciences there is the discharge of pollutants into the atmosphere or into various water systems. Margason and Fearn's reference list (ref. 1) on previous experimental investigations of incompressible jets injecting into a cross flow covers some of these research areas and, thus, provides an appropriate starting point for the present review of relevant literature.

The complex interaction that takes place after a fluid is injected into a moving stream results in a three-dimensional flow field, even though the jet may be following a two-dimensional path. (See fig. 1.) This, of course, complicates the job of experimentally measuring the complete flow field. Gordier (ref. 2), Margason (ref. 3), and Platten

and Keffer (ref. 4) concentrated their efforts on measuring the trajectory of the jet for a wide range of injection angles α_i and velocity ratios V_i/V_∞, the trajectory being one of the easiest jet properties to measure. (See fig. 2.) Jordinson (ref. 5), Keffer and Baines (ref. 6), Ramsey (ref. 7), Kamotani and Greber (ref. 8), and Fricke, Wooler, and Ziegler (ref. 9) measured details of the interaction process and revealed the very complex flow field that exists due to the pressures and shear stresses in and around the jet flow. Very good descriptions of how the jet flow distorts and develops under the influence of the free-stream flow and body forces are given by Keffer and Baines (ref. 6), Ramsey (ref. 7), Abramovich (ref. 10), and Keffer (ref. 11).

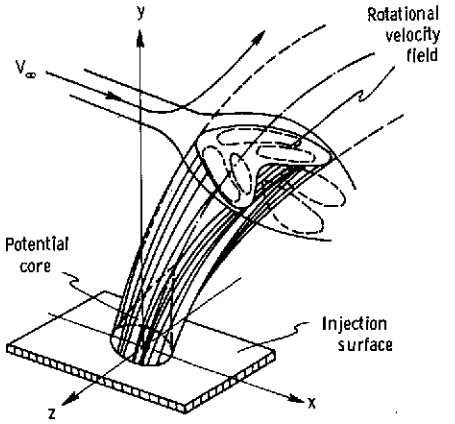

Figure 1.- Diagram of the interaction resulting from jet injection into a cross flow (after Abramovich (ref. 10)).

The most detailed measurements of the flow field appear to be those of Keffer and Baines (ref. 6) and Kamotani and Greber (ref. 8). In particular, Kamotani and Greber examine the structure of the rotational velocity field which results because of the shearing action between the free-stream flow and the edge of the jet flow. The rotational velocity field, usually interpreted to be a pair of counterrotating vortices, is an interesting as well as important facet of the injection process; it affects the path of the jet as well as the mechanisms that govern entrainment. In both reference 6 and 8, the data were reduced so that a measure of mass flux in the jet could be obtained, which in turn resulted in estimates of the rate that free-stream fluid is entrained into the jet structure. In addition to investigating the characteristics of the velocity field, Ramsey (ref. 7) and Kamotani and Greber (ref. 8) measured the temperature field resulting from the injection of a heated jet.

It is important to note the limiting conditions of a jet injected at an arbitrary angle into a cross flow. If the angle between the jet axis and the direction of the free-stream velocity α goes to zero for a given value of V_i/V_∞, the condition exists of a jet in a coflowing stream, that is, where the jet flow is parallel to the free stream. If the jet velocity becomes very large $\left(V_i/V_\infty \to \infty\right)$ for a given α, the situation approaches that of a free jet. An indication of the magnitude of entrainment for a jet in a coflowing stream and for a free jet has been provided by Morton (ref. 12) and Ricou and Spalding (ref. 13), respectively.

In reviewing some of the theoretical methods available for modeling an injection process, it should be emphasized that a method is desired here which allows the injected fluid to be followed from its point of discharge to some point downstream where complete

mixing takes place. At a minimum, from the method one should be able to estimate the three-dimensional (3-D) path of the injectant, to show how the jet size varies as it proceeds downstream, and to include basic heat-transfer mechanisms which allow the jet temperature to be predicted. The most advanced method would result in a complete and detailed description of the flow field resulting from an injection into a moving stream. This description could be accomplished by solving the full three-dimensional, turbulent, Navier-Stokes equations in an Eulerian framework, which requires the specification of the eddy viscosity field. (See ref. 14, for example.)

In order to avoid the complexities inherent with this approach, many studies have tried to theoretically model the gross features of the injection process by describing the fluid motion of the jet from the point of discharge in a Lagrangian framework. This procedure allows an estimate of jet properties to be obtained if the appropriate forces acting on the jet flow are accounted for. Since the jet path is the most obvious of the jet properties, it is natural that early attempts were concerned only with obtaining estimates of the trajectory. Abramovich (ref. 10), for example, obtained the trajectory of a jet which had a circular cross section at the injection point by balancing the centrifugal and blockage forces perpendicular to the trajectory. His basic argument was that the blockage effect of the jet flow on the free-stream flow could be approximated by assuming that the jet flow acts as a "solid" body inclined at some angle to the free stream. He accounted for the deformation of the jet cross section by assuming the shape to be elliptical and by specifying a growth rate for the cross-sectional area, which is necessary if only one force equation is used to obtain a solution for the trajectory. One of the serious drawbacks of this method is the assumption that the component of jet momentum perpendicular to the direction of the free-stream flow remains constant. This assumption was relaxed by Schetz and Billig (ref. 15).

Two other forces acting perpendicular to the jet trajectory and which help govern the development of the jet flow are (1) buoyancy force resulting from a difference in density between the jet and free-stream fluids and (2) entrainment force resulting because of the free-stream fluid that is drawn into the jet structure. Theoretical trajectories were obtained by Reilly (ref. 16) and Campbell and Schetz (ref. 17) using procedures similar to those previously described but also accounting for the entrainment phenomenon; Campbell and Schetz, in addition, included the buoyancy force in their model.

Since all these previous works utilized an assumed area growth based on experimental data obtained in the proximity of the injection point, they are not suitable for providing realistic trajectory information farther downstream. This deficiency can be avoided if, instead of assuming an area growth rate, a momentum conservation equation in the direction of the jet path is used; this equation is used in addition to the conservation equation in the direction perpendicular to the trajectory. Wooler, Burghart, and Gallagher (ref. 18), Hoult, Fay, and Forney (ref. 19), and Hoult and Weil (ref. 20) used

this procedure, solving force equations normal and parallel to the jet path simultaneously to obtain a solution for the trajectory. An added advantage of using these two force equations is that, if all the appropriate forces are accounted for, the solution procedure allows the jet flow properties to be estimated, as was done by Hirst (ref. 21) and Campbell and Schetz (ref. 22). The forces accounted for in a number of theoretical investigations are summarized in table I.

TABLE I.- CAPABILITIES OF THEORIES USING INTEGRAL TECHNIQUES

Investigation	Arbitrary injection velocity	Arbitrary injection angle	Forces parallel and perpendicular to jet trajectory			Computed jet flow properties		3-D trajectory
			Blockage	Entrainment	Buoyancy	ρ, A, V	T	
Abramovich (ref. 10)	✓	✓	✓					
Schetz & Billig (ref. 15)	✓	✓	✓					
Reilly (ref. 16)	✓		✓	✓				
Campbell & Schetz (ref. 17)	✓		✓	✓	✓			
Wooler, Burghart, & Gallagher (ref. 18)	✓		✓	✓				
Hoult, Fay, & Forney (ref. 19)	✓			✓	✓			
Hoult & Weil (ref. 20)	✓			✓	✓			
Hirst (ref. 21)	✓	✓	✓	✓	✓	✓		[a]✓
Campbell & Schetz (ref. 22)	✓	✓	✓	✓	✓	✓	✓	
Present	✓	✓	✓	✓	✓	✓	✓	✓

[a] No 3-D trajectory results given.

The theories discussed thus far have been concerned with predicting the flow characteristics of a jet following a two-dimensional (2-D) path. This type of path occurs when the radius-of-curvature vectors associated with the trajectory lie in one plane, the trajectory, of course, being a curve in that plane. If the injection and free-stream velocity vectors shown in figure 2 are considered to form an "injection plane," then a two-dimensional trajectory will always result when this plane is oriented vertically, that is, alined with the gravity vector. When the injection plane is rolled away from the vertical, a three-dimensional trajectory may occur depending on the buoyancy of the jet flow. If the buoyancy force is absent, or is small with respect to the jet momentum, then a two-dimensional path will result. A larger buoyancy force, however, will cause the jet to bend out of the injection plane, and the result will be a three-dimensional trajectory. The radius-of-curvature vectors associated with this type of trajectory do not lie in one plane. Since a jet with a two-dimensional trajectory is a special case of the jet with the more general three-dimensional trajectory, it is desirable to have a theory that can esti-

mate the more general situation. At present, the only theoretical method which appears capable of predicting jet flows with three-dimensional trajectories is that of Hirst (ref. 21), although no results of this kind were presented in his report.

In view of the preceding comments, the purpose of the present theoretical investigation is to develop an integral method which accounts for natural fluid mechanisms such as turbulence, entrainment, buoyancy, and heat transfer in the conservation equations governing the jet flow. In particular, it is desirable to have a theory that (1) utilizes the momentum conservation equation along the jet path, in addition to the one perpendicular to the path, in order to avoid any assumption regarding the growth of the jet cross-sectional area as was done in references 10 and 15 to 17; (2) obtains a third momentum conservation equation for the jet flow which, when solved simultaneously with the other two momentum equations, allows three-dimensional jet paths to be calculated, thus extending the theories reported in references 18 and 22; (3) provides estimates of the temperature of the jet fluid by examining several heat-transfer mechanisms that can account for the heat loss from the jet flow; and (4) is easily adapted to account for free-stream flows with either a nonuniform velocity field or a nonuniform temperature field.

THEORETICAL DEVELOPMENT

This section is concerned with the development of a theory which approximates the fluid mechanical process that occurs when a turbulent jet of circular cross section is injected into a semi-infinite free-stream flow. The mathematical model allows the jet to penetrate into the cross flow and to bend over and spread under the influence of natural fluidic forces, and the jet velocity vector to approach the free-stream velocity vector at some point downstream from the jet exit. This capability is obtained by considering a section of jet fluid as a control volume similar to the approach used by Reilly (ref. 16). The control volume is illustrated in figure 2 which depicts the trajectory of a jet injecting into a free-stream flow having a velocity $\vec{V}_\infty$ taken to be spatially but not time dependent. The origin of the Cartesian (x,y,z) coordinate system is at the injection point, whereas the natural (s,n,t) coordinate system moves and rotates as it follows the path of the jet axis which is traced out by the jet velocity vector. The s-axis is located along the trajectory, the n-axis is oriented perpendicular to the trajectory in the direction of the radius of curvature of the trajectory, and the t-axis is perpendicular to both the s- and n-axes and completes the right-hand axis system. A complete discussion of the natural coordinate system is given in

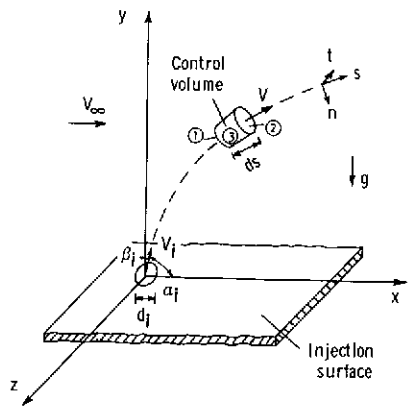

Figure 2.- Cartesian and natural coordinate systems.

appendix A. The equations expressing conservation of mass and momentum in the direction of the natural axes are derived in the following sections.

Continuity

The following integral expression equates the net influx of mass into the control volume to the rate of increase in mass in the control volume:

$$\frac{\partial}{\partial \tilde{t}} \iiint \rho_l \, d\sigma = - \iint \rho_l \vec{V} \cdot \vec{e}_N \, d\delta \tag{1}$$

where $d\delta$ and $d\sigma$ represent the elemental surface area and volume, respectively. It is assumed that the flow process is steady (in the mean), fully turbulent, and incompressible. The fact that incompressibility is assumed does not imply that the flow process is one of constant density. Equation (1) thus becomes

$$\iint \rho_l \vec{V} \cdot \vec{e}_N \, d\delta = 0 \tag{2}$$

Carrying out the operations suggested by this equation leads to the mass flows through the surfaces of the control volume (①, ②, and ③ in fig. 2).

It is noted that $d\delta = dA$ for surfaces ① and ②, which represent a cross section of the jet flow, that is, areas that are perpendicular to the trajectory. Since mass flow is a continuous single-value function of position along the trajectory, a Taylor expansion can be performed to obtain the mass flow through surface ② as a function of the mass flow through surface ①. The difference between mass flows through surfaces ① and ② represents the mass flow through the sloping face ③, which defines the amount of free-stream fluid mass (per unit of jet length) that is entrained, or drawn, into the control volume. Entrainment can be written as

$$E = \frac{d}{ds}\left[\iint_{①} \rho_l V_l \, dA\right] \tag{3}$$

The two most common profiles used in the literature to describe the velocity variation at a given cross section in the jet flow are the Gaussian and "top-hat." The Gaussian representation is particularly useful for providing estimates of flow properties on the jet center line and was used in the development of Hirst (ref. 21). In using the Gaussian profiles, however, the assumption is made that the jet flow is circular, that is, axisymmetric,

which is valid for free-jet flows and for coflowing jet flows but is questionable for a jet injecting into a cross flow where the jet cross section is not circular (ref. 6). In addition, the theoretical results obtained by using a Gaussian velocity profile are only applicable in the region where the jet flow has become fully developed.

Top-hat profiles represent the average jet flow properties and have been used in a number of theoretical studies (refs. 10, 15, 16, 18, and 20). By using the average flow properties in the conservation equations, it is not necessary to place restrictions on the symmetry of, or to assume similarity in, the jet flow. This means that the governing equations can be used to describe the jet flow in the region where the jet is fully developed or in the region where the jet is only partially developed and a potential core still exists. Accordingly, the present study uses the averaged jet flow properties defined as follows:

$$V = \frac{\iint V_l \, dA}{\iint dA} \qquad \rho = \frac{\iint \rho_l \, dA}{\iint dA} \qquad T = \frac{\iint T_l \, dA}{\iint dA} \tag{4}$$

which state that at a given location along the trajectory the jet local velocity, density, and temperature values are integrated over the jet cross-sectional area. These definitions permit the conservation of mass in the jet (eq. (3)) to be expressed in differential form as

$$E = \frac{d(\rho A V)}{ds} \tag{5}$$

Continuity equations of this form are obtained in references 12, 16, and 18.

In recent years it has been recognized that inclusion of the entrainment process in a jet injection analysis is important not only because of its influence on jet momentum, and hence trajectory, but also because this process allows for the mixing of jet and free-stream scalar properties such as temperature. The fact that entrainment occurs when there is relative motion between two flow fields has been used by different researchers to justify relating entrainment to the appropriate velocities normal and parallel to the jet axis. This type of representation of the entrainment function E results in a variety of empirical "constants" which must be adjusted in order to obtain suitable agreement with experimental data. Examples of several attempts to approximate E in this fashion are seen in references 8, 19, and 20. The model of entrainment presented in reference 18 uses three constants, one of which is obtained by satisfying the Ricou-Spalding measurements (ref. 13) for an isothermal free jet. Experiment trajectory data, rather than mass flux information, were used as the criterion for indirectly adjusting the other two con-

stants. Experimental mass flow data are presented by Kamotani and Greber in reference 8 to support the constants used in their model of the entrainment function.

Because of the complex helical streamline pattern (usually interpreted as a pair of counterrotating vortices) evident in the lee side of the jet, it is believed that the entrainment function cannot be split into two totally independent parts as described in the previous paragraph. One attempt to account for the free-stream fluid entrained into the jet as a result of the helical circulation pattern has been reported by Platten and Keffer (ref. 23). Their entrainment model was extended by Hirst (ref. 21) to account for local buoyancy in the jet flow.

In consideration of the complicated nature of analytically predicting the entrainment function and the desire to keep empirical constants to a minimum, the present study defines this jet property by using the experimental data for an air jet obtained in reference 6. The entrainment function is given by

$$E = \frac{A}{C} \rho_\infty E^* (V - V_\infty) \tag{6}$$

where C is the effective jet circumference. Equation (6) represents the entrainment parameter in functional form, where the entrainment coefficient E^* was obtained from measurements of mass flux along the jet axis (ref. 6). In order to use this formulation for E, V must always be equal to or greater than V_∞. The entrainment coefficient is presented in figure 3 for three injection velocities and, as noted, is a function of both injection velocity and distance along the trajectory. The effective velocity ratio V_{eff}, defined as the square root of the ratio of injection to free-stream dynamic pressure, has been suggested in references 3 and 8 as the proper parameter with which to compare different injection situations, and hence is utilized throughout the present paper. An empirical expression was obtained here to represent E^* in the present mathematical model and is shown compared with the experimental data. It is assumed that this function can be used at larger values of V_{eff} and s/d_i than those shown in the figure.

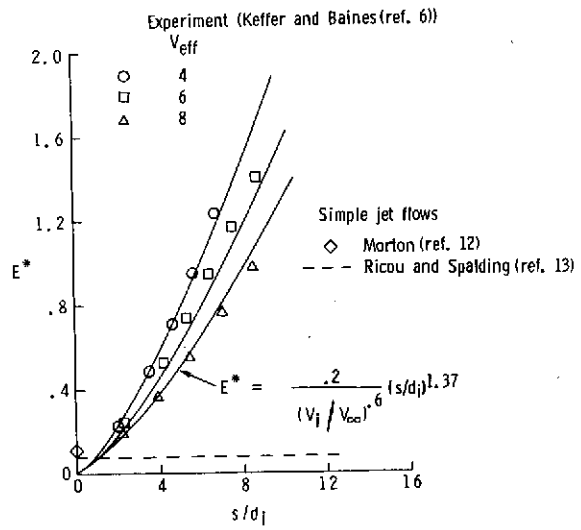

Figure 3.- Entrainment coefficient as a function of position along axis of isothermal air jet. $\alpha_i = 90^\circ$.

It should be noted that the empirical expression for E^* implies that as $s \to 0$, E^* (and hence E) $\to 0$. This is an unsettling possibility because, near $s = 0$, the jet flow in this type of injection process might

be expected to resemble that of a free jet with similar entrainment rates. Keffer and Baines (ref. 6) observed that as $s \to 0$, E^* was of the same order as that found by Morton (ref. 12) for simple jet flows. This fact is further substantiated if the work of Ricou and Spalding (ref. 13) who measured entrainment for axisymmetric turbulent free-jets is considered. The formula they suggested as best representing their data is

$$\frac{\rho A V}{(\rho a V)_i} = 0.32 \frac{s}{d_i} \tag{7}$$

This equation can be differentiated with respect to s to get the entrainment in the free jet. Putting the results in the same form used by Morton gives

$$E = 0.08 C_i \rho_i V_i \tag{8}$$

Thus, the constant 0.08 compares favorably with Morton's value of 0.116.

It is assumed in the present study that $E^* = 0.08$ until the empirical expression presented in figure 3 predicts a greater value, which is then used. This is reasonable in view of the fact that an increase in V_{eff} decreases E^* so that as $V_{eff} \to \infty$, E^* should approach the free-jet value.

Conservation of Momentum

The following integral expression equates the rate of increase of momentum in the control volume to the sum of forces acting on the control volume plus the net influx of momentum into the control volume:

$$\frac{\partial}{\partial t} \iiint \rho_l \vec{V} \, d\sigma = \iiint \vec{f}_b \, d\sigma + \iint \vec{\vec{\tau}} \cdot \vec{e}_N \, d\delta - \iint \vec{V} \left(\rho_l \vec{V} \cdot \vec{e}_N \right) d\delta \tag{9}$$

where the surface stress tensor $\vec{\vec{\tau}}$ is taken to contain both shear and pressure terms and $\vec{f}_b \equiv$ Body force per unit volume. Since a time independent flow process has been assumed, the term on the left-hand side of equation (9) is zero; hence,

$$\iiint \vec{f}_b \, d\sigma + \iint \vec{\vec{\tau}} \cdot \vec{e}_N \, d\delta - \iint \vec{V} \left(\rho_l \vec{V} \cdot \vec{e}_N \right) d\delta = 0 \tag{10}$$

This equation will be used to obtain expressions for momentum in the direction of the natural coordinates.

Assuming the body forces are independent of the integral over $d\sigma$ gives

$$\iiint \vec{f}_b \, d\sigma = \vec{f}_b \iiint d\sigma = \vec{f}_b A \, \Delta s \tag{11}$$

where, as a first approximation, the volume is assumed to be equal to $A \, \Delta s$, which neglects the rate of change of A with s. The length of the jet control volume is represented by Δs. Since the components of $\vec{f}_b$ and later $\vec{V}_\infty$ are desired in the s-, n-, and t-directions, a vector identity can be used to obtain

$$\vec{f}_b = \left(\vec{f}_b \cdot \vec{e}_s\right)\vec{e}_s + \left(\vec{f}_b \cdot \vec{e}_n\right)\vec{e}_n + \left(\vec{f}_b \cdot \vec{e}_t\right)\vec{e}_t \tag{12}$$

and

$$\vec{V}_\infty = \left(\vec{V}_\infty \cdot \vec{e}_s\right)\vec{e}_s + \left(\vec{V}_\infty \cdot \vec{e}_n\right)\vec{e}_n + \left(\vec{V}_\infty \cdot \vec{e}_t\right)\vec{e}_t \tag{13}$$

where $\vec{V}_\infty = V_\infty \vec{e}_x$.

There are two body forces considered to be acting on the jet flow. The first force is due to the buoyant condition which results from a difference in density between the jet and free-stream fluids. This force acts in the y-direction and is given by

$$\vec{f}_g = f_g \vec{e}_y = g\left(\rho_\infty - \rho\right)\vec{e}_y \tag{14}$$

The second force results from centrifugal effects associated with the jet having mass and following a curved path. This force acts in the direction of the radius of curvature of the trajectory and is expressed as

$$\vec{f}_c = f_c \vec{e}_n = \frac{-\rho V^2}{R} \vec{e}_n \tag{15}$$

The total body force per unit volume on the control volume $\vec{f}_b$ is the vector sum of the buoyancy and centrifugal forces and is substituted into equation (12) to obtain

$$\vec{f}_b = f_g\left(\vec{e}_y \cdot \vec{e}_s\right)\vec{e}_s + \left[f_g\left(\vec{e}_y \cdot \vec{e}_n\right) + f_c\right]\vec{e}_n + f_g\left(\vec{e}_y \cdot \vec{e}_t\right)\vec{e}_t \tag{16}$$

The pressure portion of the shear-stress tensor term in equation (10) can be written in component form as

$$\iint p\vec{e}_N \, d\delta = -\iint_{(1)} p_l \vec{e}_s \, d\delta + \iint_{(2)} p_l \vec{e}_s \, d\delta + \iint_{(3)} p_l \vec{e}_n \, d\delta$$
$$+ \iint_{(3)} p_l \vec{e}_t \, d\delta - \iint_{(3)} p_l \vec{e}_s \, d\delta \tag{17}$$

where p_l represents the local pressure on the respective surfaces indicated by the integration.

n-momentum.- The n-momentum equation is obtained by taking the n-components of the various vector quantities in the momentum integral equation (10). The term representing the body forces, for example, is extracted from equation (16) as

$$f_{b,n} = f_g\left(\vec{e}_y \cdot \vec{e}_n\right) + f_c \tag{18}$$

and the pressure force is obtained from equation (17) to be

$$F_{p,n} = \iint_{(3)} p_l \, d\delta \tag{19}$$

This pressure force is combined with the shear stress integrated over surface (3) to obtain the total drag force D_n on the jet flow due to blockage of the free-stream flow. It is noted that for many injection situations the centrifugal force is in the opposite direction from the drag force, the drag force being in the positive n-direction.

Because of the complexity of the interaction between the jet and free-stream flows, the force resulting from the blockage effect is postulated to be the drag on an equivalent "solid" cylindrical jet shape inclined at an angle to the free-stream flow (after Abramovich (ref. 10)). This force can be expressed as

$$D_n = C_{D,n} q_{\infty,n} S_{ref,n} \tag{20}$$

where the dynamic pressure of the free-stream flow perpendicular to the jet axis is given by

$$q_{\infty,n} = \frac{1}{2} \rho_\infty V_{\infty,n}^2 \tag{21}$$

Employing the definition $V_{\infty,n} = V_\infty\left(\vec{e}_x \cdot \vec{e}_n\right)$ results in

$$q_{\infty,n} = q_{\infty}\left(\vec{e}_x \cdot \vec{e}_n\right)^2 \tag{22}$$

The reference area for calculating the drag force is defined by

$$S_{ref,n} = h\,\Delta s \tag{23}$$

where h is the local width of the jet measured in the t-direction. Incorporating the expressions for $q_{\infty,n}$ and $S_{ref,n}$ into equation (20) allows the drag force to be finally expressed as

$$D_n = C_{D,n} q_{\infty}\left(\vec{e}_x \cdot \vec{e}_n\right)^2 h\,\Delta s \tag{24}$$

The third term in equation (10) accounts for the net influx of momentum into the control volume, which for the n-direction, is due solely to the flux across the slanted surface of the cylinder. It is represented by the rate at which mass enters the sides of the control volume (eq. (3)) multiplied by the free-stream velocity component in the n-direction. Thus,

$$\vec{e}_n \cdot \iint \vec{V}\left(\rho_l \vec{V} \cdot \vec{e}_N\, d\delta\right) = V_{\infty,n} \frac{\partial}{\partial s}\left[\iint \rho_l V_l\, dA\right]\Delta s = V_{\infty,n} E\,\Delta s \tag{25}$$

Integrating equation (18) over the control volume and combining the results with equations (24) and (25) yield the following conservation of momentum equation in the n-direction:

$$\frac{\rho A V^2}{R} = g\left(\rho_{\infty} - \rho\right)\left(\vec{e}_y \cdot \vec{e}_n\right)A + C_{D,n} q_{\infty} h\left(\vec{e}_x \cdot \vec{e}_n\right)^2 + E V_{\infty}\left(\vec{e}_x \cdot \vec{e}_n\right) \tag{26}$$

The expressions for the dot products in terms of the Cartesian coordinates as the dependent variables and the distance along the trajectory as the independent variable are given in appendix A. Substituting the appropriate definitions the n-momentum equation becomes

$$\frac{\rho A V^2}{R} = gA\left(\rho_{\infty} - \rho\right)R \frac{d^2y}{ds^2} + C_{D,n} q_{\infty} h R^2 \left(\frac{d^2x}{ds^2}\right)^2 + E V_{\infty} R \frac{d^2x}{ds^2} \tag{27}$$

where the radius of curvature R of the trajectory is defined in appendix A. Previous studies of the 2-D injection problem (usually vertical injection) proceed to put this equation into a form with the slope of the trajectory, or the angular orientation, as the depend-

ent variable. Since the vertical and lateral injection problems are treated herein as special cases of the more general 3-D injection situation, it is desirable not to specialize the equations in that way. The reader will see in appendix B how this equation is nondimensionalized and put into the form used in obtaining a numerical solution on the computer. The direction cosines of the jet velocity vector (i.e., $\vec{e}_s$) were chosen as the dependent variables for several reasons, one of which is that the order of the governing equations is reduced by one. In addition, the algebra is thereby kept to a manageable level.

It is appropriate to mention that at this stage of the development, the approach used in a number of previous studies (refs. 10 and 15 to 17) has been to assume the area growth of the jet along the trajectory, the rate of growth being based on data measurements where $s/d_i \leq 10$. This was done in lieu of solving the s-momentum equation. The area growth can be obtained by assigning a certain shape for the jet cross section (e.g., circular or elliptical) and by allowing the jet width to grow at a specified rate. Schetz and Billig (ref. 15) used the expression for mass flow in the jet, that is, the continuity equation, to eliminate velocity in the n-momentum equation, the resulting expression then being integrated to obtain a solution for the jet trajectory. Typical results obtained by this procedure are presented in figure 4 for a jet with an elliptical cross-sectional shape and are compared with experimental data acquired from the photographs in reference 17.

Comparison of the assumed cross-sectional areas with the values obtained from experiments shows that the two are in reasonable agreement in the proximity of the jet exit but that the values diverge as the jet proceeds downstream, the measured areas indicating a much more rapid rate of jet growth than the assumed values. This trend is reflected in the trajectory information where good agreement between the predicted and experimental trajectories is noted in the initial region after jet injection, but poorer agreement occurs farther downstream. It should be mentioned that the investigators who made the area-growth assumption were predominantly interested in the jet trajectory in the proximity of the injection point. Another effect of assuming area growth is seen in the erroneous trends for the theoretical jet velocity, illustrated in figure 4 by the velocity deficit curve. As noted, the jet velocity begins to increase at some point along the trajectory. The reader is aware, of course, that as long as the jet injection velocity is greater than the free-stream velocity, the jet velocity will decrease continuously along the trajectory and eventually approach the free-stream velocity value far downstream.

From these remarks it is obvious that an alternative approach should be considered such that the jet cross-sectional area is permitted to be an unknown in the governing equations. In order to do this it is necessary to have another equation to solve along with the continuity and n-momentum equations. The equation expressing conservation of momentum along the trajectory satisfies this need. By using this additional momentum equation, a more natural description of the jet flow properties is obtained as illustrated in figure 4.

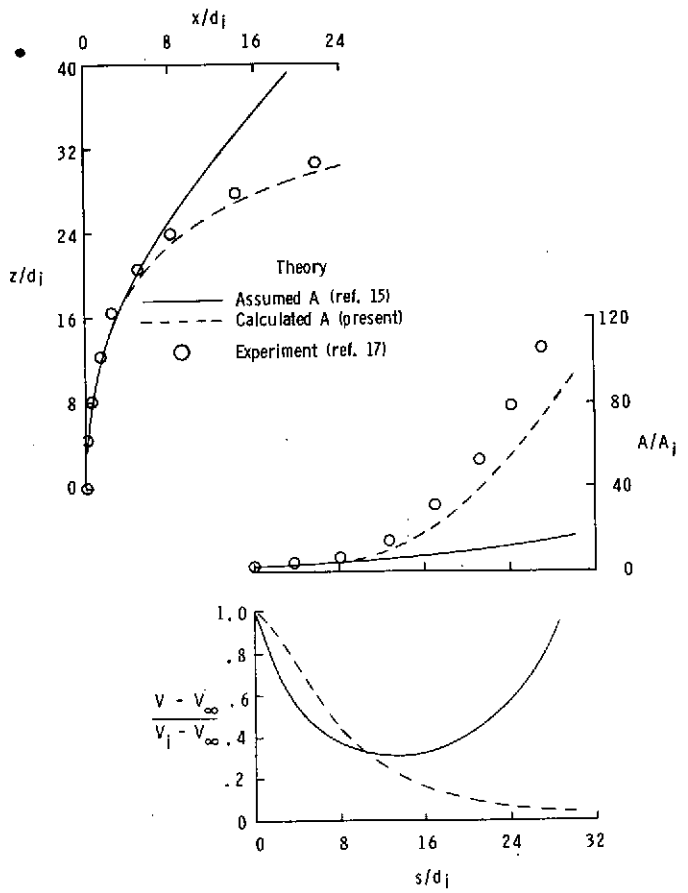

Figure 4.- Experimental and theoretical jet flow properties for a water injection process. $V_{eff} = 18.2$; $T_j/T_\infty = 1.0$; $\alpha_i = 90^\circ$.

Although the area assumption is to be discarded, it is still necessary to provide information concerning the width of the jet in order to calculate the drag terms in the governing equations. One approach is to follow Abramovich (ref. 10) and assume the growth of the jet width along the trajectory by using an empirical expression based on limited experimental data. Another approach is to specify a shape for the jet cross section and to use this with the computed area to calculate the jet width. This latter approach is more appealing because it is easier to justify its use on the basis of available experimental data. Keffer and Baines (ref. 6), for example, have shown that a jet initially having a circular cross section transforms to a "kidney" shape as the jet penetrates into the cross flow. This shape remains approximately the same with increase in s as illustrated in figure 5.

Prior attempts by researchers at approximating the jet cross section have been limited to the elliptical shape, where the circle is a degenerate case. Hirst (ref. 21),

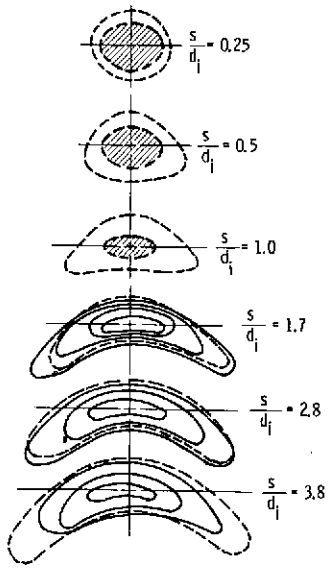

Figure 5.- Cross-sectional pressure contours of jet injected normally into cross flow, $V_j/V_\infty = 2.2$ (after Abramovich (ref. 10)). Solid and dashed lines represent lines of constant total and static pressure, respectively; shaded areas indicate potential core region.

for example, approximated the jet cross section as a circle, which was a useful assumption in his development because then he assumed the jet flow to be axisymmetric. It would appear that the ellipse would be a more suitable approximation, particularly near the injection point where the jet flow is deformed by the large pressure and shear stress fields. An ellipse with a major-to-minor axis ratio of 5:1 was employed in reference 10 and later in references 15 to 17, whereas reference 18 assumed a 4:1 ellipse. The approximation used in reference 18 had the added advantage of accounting for the change from the circular shape at the jet exit to the 4:1 ellipse at a specified point along the trajectory.

For the present study, the jet cross-section shape is assumed to be elliptical with a ratio of major-to-minor axes of 5:1, the major axis being the jet width. It is also assumed that at the injection point ($s = 0$) the elliptical area is equal to that of a circle with diameter d_j. The change of jet width h along the trajectory is accounted for by the expression

$$h = \sqrt{\frac{20A}{\pi}} \tag{28}$$

The change in h with distance along the trajectory was obtained by using calculated values of A resulting from the solution of the governing conservation equations. This variation is shown in figure 6 compared with experimental data obtained from Kamotani and Greber (ref. 8). The data points from reference 8 were obtained from contours of con-

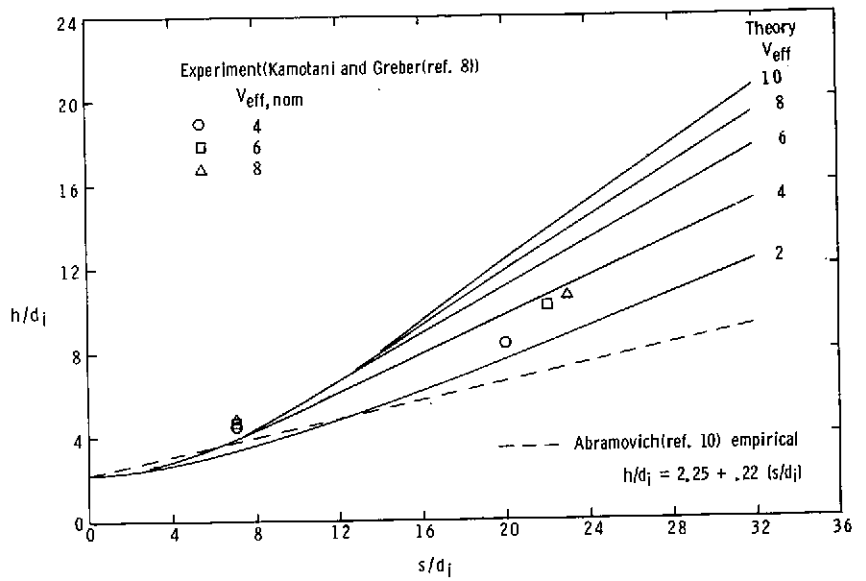

Figure 6.- Variation of jet width with distance along trajectory for a range of injection velocities. $\alpha_j = 90^\circ$; $T_j/T_\infty = 1.0$.

stant velocity normal to a jet cross section, where the velocity excess had decreased to 10 percent of the maximum excess. The theory predicts the trend of increase in h/d_j with increase in s/d_j, although the predicted values are higher than the measured values at large s/d_j. The small effect of V_{eff} on h/d_j near the injection point is reflected by the theory. The empirical expression used by Abramovich (ref. 10) in his theory is shown for comparison.

The value of $C_{D,n}$ associated with the 5:1 elliptical shape is taken to be 1.6 in keeping with the equivalent "solid" body argument and is assumed to be independent of the Reynolds number of the flow over the ellipse $N_{Re,d}$. Wooler, Burghart, and Gallagher (ref. 18) used a value of 1.8 in their analysis, whereas Abramovich (ref. 10) used 3.0, a value which was pointed out by Schetz and Billig (ref. 15) as being totally unrealistic. An indication of how sensitive the theory is to the choice of cross-section shape and blockage coefficient can be seen in figure 7 where experimental and theoretical trajectory results are compared for $V_{eff} = 4.0$. The effect of changing ellipse axis ratio is presented in figure 7(a) where $C_{D,n} = 1.6$ is used in the theoretical calculations, whereas the effect of varying $C_{D,n}$ for a specific ellipse axis ratio (5:1) is shown in figure 7(b). As noted, increasing either ellipse axis ratio or blockage coefficient results in progressively lower theoretical trajectories. The trends discussed here for $V_{eff} = 4.0$ are typical of other injection velocities. The fact that the theoretical results obtained for $C_{D,n} = 1.8$ (fig. 7(b)) are in better agreement with the experimental trajectories than the results obtained for $C_{D,n} = 1.6$ is misleading. It will be demonstrated later (fig. 22) that the theory estimates mass flows in the jet that are too low, so that if this disparity was

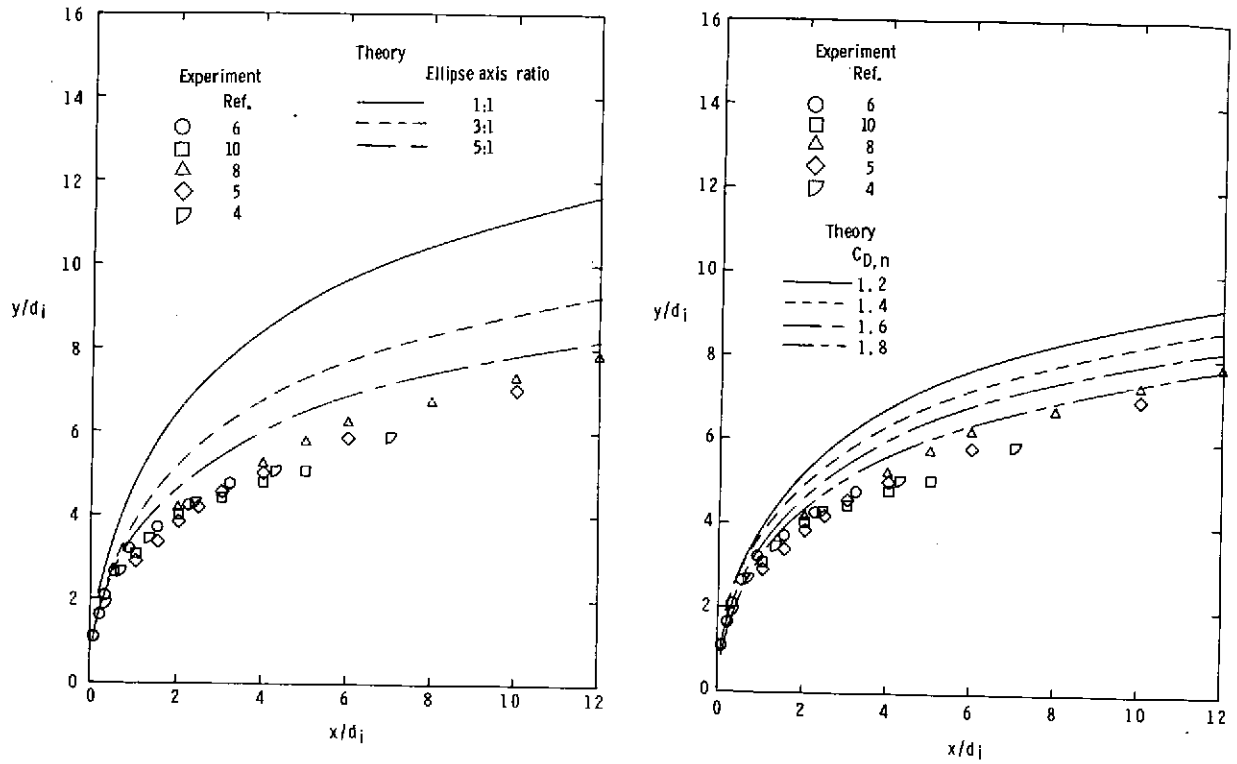

(a) $C_{D,n} = 1.6$.

(b) 5:1 ellipse.

Figure 7.- Effect of jet cross-sectional shape and blockage coefficient on theoretical trajectories for $V_{eff} = 4.0$. $\alpha_j = 90°$; $\beta_j = 0°$.

corrected the results obtained with $C_{D,n} = 1.6$ would show improved agreement with the experiment.

s-momentum.- The s-momentum equation is obtained by taking the s-components of the various vector quantities in equation (10). The resulting expression represents a balance between the rate of change of jet momentum and the forces on the jet due to changes in mean jet pressure, to buoyancy caused by density differences between the jet and free-stream fluids and to entrainment of ambient fluid into the jet.

In the s-direction the shear and pressure forces are not combined as they were in the n-direction. The appropriate pressure force acquired from equation (17) is

$$F_{p,s} = -\underset{①}{\iint} p_l \, d\delta + \underset{②}{\iint} p_l \, d\delta - \underset{③}{\iint} p_l \, d\delta \tag{29}$$

where the local pressures are integrated over the control surface to get

$$F_{p,s} = -\bar{p}_{(1)}A_{(1)} + \bar{p}_{(2)}A_{(2)} - \bar{p}_{(3)}A_{(3)} \tag{30}$$

A Taylor expansion can be performed to obtain the pressure and area at surface (2) in terms of the appropriate variables at surface (1), whereas $\bar{p}_{(3)}$ is taken to be the average of $\bar{p}_{(1)}$ and $\bar{p}_{(2)}$ and $A_{(3)}$ to be the difference between $A_{(1)}$ and $A_{(2)}$. Substituting these expressions into equation (30), neglecting terms having higher orders of ds, gives the pressure force in the s-direction as

$$F_{p,s} = A\frac{\partial \bar{p}}{\partial s}\Delta s \tag{31}$$

The force contribution of the surface stress tensor in the s-direction is zero because the local jet velocity at the control volume surface is equal to the free-stream velocity component tangent to the jet flow, thus negating a shearing stress.

The contribution of the net influx of momentum into the control volume to the force balance in the s-direction is obtained by performing the operations suggested by the third term in equation (10) and is found to be

$$\vec{e}_s \cdot \iint \vec{V}\left(\rho_l \vec{V} \cdot \vec{e}_N \, d\delta\right) = \frac{\partial}{\partial s}\left(\rho A V^2\right)\Delta s - EV_\infty\left(\vec{e}_x \cdot \vec{e}_s\right)\Delta s \tag{32}$$

The definition of averaged jet properties was used to derive this equation, and the momentum flux entering the sloping surface of the control volume was represented by the rate that mass flows across the surface multipled by the free-stream velocity component in the s-direction. Equations (31) and (32) are combined with the body force term from equation (16) and the dot product expressions from appendix A to obtain the following s-momentum equation:

$$\frac{\partial\left(\rho A V^2\right)}{\partial s} = gA\left(\rho_\infty - \rho\right)\frac{dy}{ds} - A\frac{\partial \bar{p}}{\partial s} + EV_\infty \frac{dx}{ds} \tag{33}$$

In order to evaluate the static pressure gradient along the trajectory $\left(\partial\bar{p}/\partial s\right)$, the assumption is made that the free-stream static-pressure field around the jet perimeter imposes itself on the jet flow. This is the usual type of assumption made concerning other free turbulent processes, such as jet injection parallel to a mainstream (coflowing flow) or jet injection into a reservoir (free jet flow). For the present case where the jet structure is considered as an elliptical cylinder inclined at an angle to the free-stream flow, there are large variations in the free-stream pressure field around the jet due to

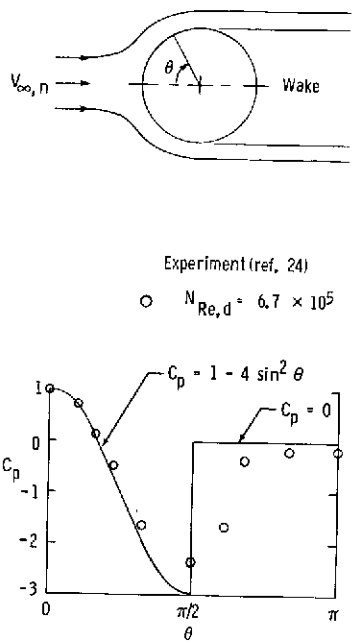

Figure 8.- Static pressure variation around the perimeter of a circular cylinder.

the blockage effect that the jet has on the free-stream flow. Some idea of the static pressure variation around the perimeter of a jet cross section, idealized as a circular cylinder, can be obtained by observing the experimental pressures in figure 8. (These experimental pressures were obtained from ref. 24.) An assumed pressure distribution to be used in the theory is also presented. As noted, the assumed pressures on the front of the cylinder $\left(0 \leqq \theta \leqq \frac{\pi}{2}\right)$ are in functional form and were obtained from potential flow theory, whereas the pressures on the back of the cylinder $\left(\frac{\pi}{2} < \theta \leqq \pi\right)$ are assumed to be equal to the free-stream pressure. Several researchers (e.g., Ramsey (ref. 7) and Kamotani and Greber (ref. 8)) have approximated the pressure field around the jet by examining the potential flow over various cylindrical shapes. Although the pressure field resulting from the turbulent jet injection process is very complicated and does not lend itself to be categorized in this simple a fashion, the pressure variation in figure 8 is adequate for use in the present mathematical model. The local surface pressure $\left(C_p q_{\infty,n} + p_\infty\right)$ is used in the expression

$$\bar{p} = \frac{\int_0^\pi p \, d\theta}{\int_0^\pi d\theta} \tag{34}$$

to obtain the average static pressure acting on the cylinder. Performing the integrations in equation (34) with the pressure distribution shown in figure 8 gives

$$\bar{p} = p_\infty - \frac{1}{2} q_{\infty,n} \tag{35}$$

where it is recalled that $q_{\infty,n}$ is the dynamic pressure resulting from the free-stream velocity component normal to the trajectory. (See eq. (22).) This equation implies that the average static pressure on the jet cross section is less than the free-stream static pressure but approaches p_∞ as $q_{\infty,n}$ approaches zero. This occurs when V_∞ approaches zero and/or when the jet becomes parallel to the free-stream flow (i.e.,

$\alpha = 0$). If the average pressure is assumed to impose itself on the jet flow (i.e., the pressure in the jet flow becomes $\bar{p}$), $\bar{p}$ can be differentiated with respect to s to get

$$\frac{d\bar{p}}{ds} = -q_\infty \left[R \frac{dR}{ds} \left(\frac{d^2x}{ds^2} \right)^2 + R^2 \frac{d^2x}{ds^2} \frac{d^3x}{ds^3} \right] \tag{36}$$

It is noted that if the jet trajectory is in either the vertical (X-Y) or lateral (X-Z) planes, the expression for the pressure gradient (eq. (36)) simplifies to

$$\frac{d\bar{p}}{ds} = -q_\infty \sin \alpha \cos \alpha \frac{d\alpha}{ds} \tag{37}$$

which is the form used by Campbell and Schetz (ref. 22). Incorporating the pressure gradient term (eq. (36)) into equation (33) yields the following final form of the s-momentum equation:

$$\frac{\partial(\rho A V^2)}{\partial s} = gA(\rho_\infty - \rho)\frac{dy}{ds} + q_\infty A \left[R \frac{dR}{ds} \left(\frac{d^2x}{ds^2} \right)^2 + R^2 \frac{d^2x}{ds^2} \frac{d^3x}{ds^3} \right] + EV_\infty \frac{dx}{ds} \tag{38}$$

t-momentum.- The t-momentum equation is obtained by taking the t-components of the various vector quantities in equation (10). The resulting expression represents a balance of forces on the control volume due to buoyancy, to blockage of the free-stream flow, and to entrainment of ambient fluid into the jet. Similar to the derivation of the n-momentum equation, the pressure force is combined with the shear stress integrated over surface (3) to obtain the total force D_t acting on the jet in the t-direction. Accordingly,

$$D_t = C_{D,t} q_{\infty,t} S_{ref,t} \tag{39}$$

where

$$q_{\infty,t} = q_\infty \left(\vec{e}_x \cdot \vec{e}_t \right)^2 \tag{40}$$

If the jet cross section were circular, then $C_{D,t}$ would equal $C_{D,n}$ and $S_{ref,t}$ would equal $S_{ref,n}$. However, since the shape is elliptic and not circular, $C_{D,t}$ is not equal to $C_{D,n}$ and $S_{ref,t}$ is not equal to $S_{ref,n}$. Since the elliptical shape has an axis ratio of 5:1, $S_{ref,t} = \frac{h}{5} \Delta s$, so that

$$D_t = C_{D,t} q_\infty \left(\vec{e}_x \cdot \vec{e}_t\right)^2 \frac{h}{5} \Delta s \tag{41}$$

where $C_{D,t}$ is taken to be 1.0.

The net flux of momentum in the t-direction entering through the sloping surface of the control volume is represented by the rate at which mass flows across the surface multiplied by the free-stream velocity component in the t-direction; this results in

$$\vec{e}_t \cdot \iint \vec{V}\left(\rho_l \vec{V} \cdot \vec{e}_t \, d\delta\right) = EV_\infty \left(\vec{e}_x \cdot \vec{e}_t\right) \Delta s \tag{42}$$

The body force term from equation (16) is combined with equations (41) and (42) to obtain the t-momentum equation:

$$gA\left(\rho_\infty - \rho\right)\left(\vec{e}_y \cdot \vec{e}_t\right) + C_{D,t} \frac{h}{5} q_\infty \left(\vec{e}_x \cdot \vec{e}_t\right)^2 + EV_\infty \left(\vec{e}_x \cdot \vec{e}_t\right) = 0 \tag{43}$$

After substituting for the dot products (appendix A), the torsion τ_o associated with the trajectory is arranged so that it is in the numerator of the terms. The reason for this arrangement is that τ_o is expected to have a small value for the present study ($\tau_o = 0$ for a two-dimensional trajectory). The resulting expression is

$$\begin{aligned}
&\tau_o gA\left(\rho_\infty - \rho\right)\frac{dR}{ds}\frac{d^2y}{ds^2} + \tau_o gA\left(\rho_\infty - \rho\right)R\frac{d^3y}{ds^3} + \tau_o \frac{gA}{R}\left(\rho_\infty - \rho\right)\frac{dy}{ds} \\
&+ C_{D,t} q_\infty \frac{h}{5}\left(\frac{dR}{ds}\right)^2\left(\frac{d^2x}{ds^2}\right)^2 + C_{D,t} q_\infty \frac{h}{5} R^2\left(\frac{d^3x}{ds^3}\right)^2 + C_{D,t} \frac{q_\infty h}{5R^2}\left(\frac{dx}{ds}\right)^2 \\
&+ \frac{2}{5} C_{D,t} q_\infty hR \frac{dR}{ds}\frac{d^2x}{ds^2}\frac{d^3x}{ds^3} + \frac{2}{5} C_{D,t} q_\infty h \frac{dx}{ds}\frac{d^3x}{ds^3} + \frac{2}{5} C_{D,t} q_\infty \frac{h}{R}\frac{dR}{ds}\frac{d^2x}{ds^2}\frac{dx}{ds} \\
&+ \tau_o EV_\infty \frac{dR}{ds}\frac{d^2x}{ds^2} + \tau_o EV_\infty R\frac{d^3x}{ds^3} + EV_\infty \frac{\tau_o}{R}\frac{dx}{ds} = 0
\end{aligned} \tag{44}$$

For the case where the jet follows a two-dimensional path, the t-momentum equation is an identity (see appendix B); hence, its use is not necessary in the procedure for obtaining a solution of the jet trajectory and flow properties.

Heat Energy

Until this point only the mass and momentum aspects of the jet injection process have been discussed; however, since the present investigation is concerned with heated discharges, it is necessary to also consider appropriate methods of describing the thermal characteristics of the flow. In particular, it is advantageous to determine the change in mean jet temperature resulting from the penetration of the jet into the cross flow. This determination can be accomplished by monitoring the heat loss from the control volume, the heat loss resulting from several heat-transfer mechanisms.

The first type of heat-transfer mechanism pertains to the reduction in energy content per unit volume $\rho c_p T$ of the jet fluid due to the entrainment of free-stream fluid at a different energy level $\left(\rho c_p T\right)_\infty$. Applying this concept to the control volume results in the expression

$$\left(mc_pT\right)_2 = \left(mc_pT\right)_1 + m_e\left(c_pT\right)_\infty \tag{45}$$

where $\left(mc_pT\right)_1$ represents the energy level in the control volume that would exist if there were no entrainment and $\left(mc_pT\right)_2$ represents the equilibrium energy level resulting from the complete mixing of the jet and entrained fluids. The various specific heats in equation (45) are assumed to have the same value.

Forced convection, the second type of heat-transfer mechanism being considered, results when the free stream flows around the heated jet fluid and extracts heat energy from the jet in the process. This heat transfer is analogous to the forced convection in separated flow over a heated cylinder, where the cylinder is cooled by the fluid flowing normal to the cylinder axis. To be consistent with our previous approach, the convective heat transfer is estimated by considering the jet structure as a cylinder inclined at an angle to the free-stream flow.

Eckert and Drake (ref. 25) give several examples of film heat-transfer coefficients occurring in this type of flow situation and suggest the following expression for estimating an average Nusselt number:

$$N_{Nu,d} = 0.43 + 1.11\psi\left(N_{Re,d}\right)^{\xi}\left(N_{Pr}\right)^{0.31} \tag{46}$$

The value of Prandtl number for an air injection process is taken to be 1.0, whereas for a water injection process the functional dependence of N_{Pr} on water temperature was obtained from tables in reference 25. The Reynolds number is defined with the "effective" diameter of the jet as the reference length and the free-stream velocity component per-

pendicular to the jet axis as the reference velocity so that Nusselt number will be sensitive to the changes in local flow conditions as the jet penetrates into the cross flow. The Reynolds number is thus

$$N_{Re,d} = \frac{\rho_\infty V_{\infty,n} d}{\mu_\infty} = \frac{dV_\infty R}{\nu_\infty} \frac{d^2x}{ds^2} \tag{47}$$

For vertical or lateral injection this equation reduces to

$$N_{Re,d} = \frac{dV_\infty}{\nu_\infty} \sin \alpha \tag{48}$$

The values of $N_{Re,d}$ occurring in the present study suggest the selection of $\psi = 0.45$ and $\xi = 0.50$ for use in equation (46).

The definition of Nusselt number is Hd/k where k represents the thermal conductivity of the jet fluid. This definition is used to obtain the average film heat-transfer coefficient H which yields the following rate of heat loss from the jet fluid:

$$Q = HS_c(T_\infty - T) \tag{49}$$

where S_c denotes the cylindrical area of the jet control volume. This, in turn, results in a temperature change in the jet flow due to this convective heat loss.

An example of the temperature results obtained when these two heat-transfer mechanisms are incorporated into the solution of the governing conservation equations is shown in figure 9, where the theoretical calculations were made with the same injection conditions as the water injection process reported in reference 22. The trend of temperature decrease along the trajectory measured in reference 22 is adequately estimated by the theory, the predicted average temperature values falling below the measured maximum temperatures. These results are substantiated by the temperature data for air injection processes measured by Ramsey (ref. 7) and Kamotani and Greber (ref. 8). The theoretical temperatures obtained by considering only the effects of entrainment are presented to demonstrate the relative magnitudes of the two types of heat-transfer mechanisms. Convection is seen to be the dominant mechanism

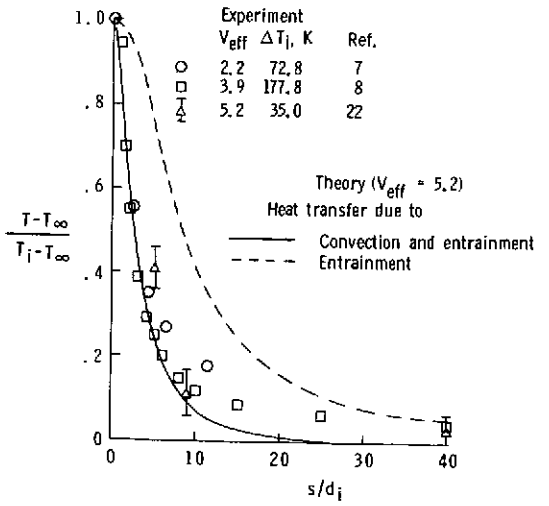

Figure 9.- Variation of jet temperature with distance along trajectory for heated injection process. $T_i > T_\infty$.

for determining temperature loss in the early stages of the jet injection process, whereas the effects of entrainment become dominant as the jet proceeds downstream.

Solution Procedure

This section summarizes the highly nonlinear governing differential equations and briefly describes the iterative method that is employed to obtain a numerical solution at specific locations along the jet trajectory. Appendix B shows how the equations are nondimensionalized and put into the forms used in the numerical technique. The governing equations are repeated here for convenience as follows:

Continuity (eq. (6)):

$$E = \frac{A}{C} \rho_\infty E^* (V - V_\infty)$$

n-momentum (eq. (27)):

$$\frac{\rho A V^2}{R} = gA(\rho_\infty - \rho)R \frac{d^2y}{ds^2} + C_{D,n} q_\infty h R^2 \left(\frac{d^2x}{ds^2}\right)^2 + EV_\infty R \frac{d^2x}{ds^2}$$

s-momentum (eq. (38)):

$$\frac{\partial(\rho A V^2)}{\partial s} = gA(\rho_\infty - \rho)\frac{dy}{ds} + q_\infty A\left[R \frac{dR}{ds}\left(\frac{d^2x}{ds^2}\right)^2 + R^2 \frac{d^2x}{ds^2}\frac{d^3x}{ds^3}\right] + EV_\infty \frac{dx}{ds}$$

t-momentum (eq. (44)):

$$\tau_o gA(\rho_\infty - \rho)\frac{dR}{ds}\frac{d^2y}{ds^2} + \tau_o gA(\rho_\infty - \rho)R\frac{d^3y}{ds^3} + \tau_o \frac{gA}{R}(\rho_\infty - \rho)\frac{dy}{ds}$$

$$+ C_{D,t} q_\infty \frac{h}{5}\left(\frac{dR}{ds}\right)^2\left(\frac{d^2x}{ds^2}\right)^2 + C_{D,t} q_\infty \frac{h}{5} R^2\left(\frac{d^3x}{ds^3}\right)^2 + C_{D,t}\frac{q_\infty h}{5R^2}\left(\frac{dx}{ds}\right)^2$$

$$+ \frac{2}{5} C_{D,t} q_\infty h R \frac{dR}{ds}\frac{d^2x}{ds^2}\frac{d^3x}{ds^3} + \frac{2}{5} C_{D,t} q_\infty h \frac{dx}{ds}\frac{d^3x}{ds^3} + \frac{2}{5} C_{D,t} q_\infty \frac{h}{R}\frac{dR}{ds}\frac{d^2x}{ds^2}\frac{dx}{ds}$$

$$+ \tau_o EV_\infty \frac{dR}{ds}\frac{d^2x}{ds^2} + \tau_o EV_\infty R \frac{d^3x}{ds^3} + EV_\infty \frac{\tau_o}{R}\frac{dx}{ds} = 0$$

Heat transfer due to

entrainment (eq. (45)):

$$(mc_pT)_2 = (mc_pT)_1 + m_e(c_pT)_\infty$$

convection (eq. (49)):

$$Q = HS_c(T_\infty - T)$$

It was found that the s-, n-, and t-momentum equations could be simplified somewhat by using direction cosines u and w as the dependent variables rather than x, y, and z. This procedure means that at each point $j+1$ on the trajectory a solution to this initial value problem involves determining values for u_{j+1}, w_{j+1}, ρ_{j+1}, A_{j+1}, and V_{j+1}.

The basic solution procedure is to solve the s-momentum equation for the jet momentum in the control volume, where the coefficients in that equation are estimated by using the flow property values obtained from the solution at the previous location on the trajectory. The s-momentum equation is used in conjunction with the continuity equation to provide an update on V_{j+1}, and the heat loss from the control volume is calculated to provide new estimates for T_{j+1} and ρ_{j+1}. The current flow property values are then used in the coefficients of the n-momentum equation to obtain a solution for $(du/ds)_{j+1}$ where a central difference scheme provides u_{j+2}. Iteration between the s- and n-momentum equations provides the information used to solve the t-momentum equations for $(d^2w/ds^2)_{j+1}$, from which w_{j+2} is obtained by using a central-difference scheme. The most recently calculated values of the direction cosines and flow properties are used to iterate back through the governing equations. (See flow chart of iteration process in fig. 10.) For the case where the jet path is two dimensional the information from the t-momentum equation is redundant; therefore, it is only necessary to solve the s- and n-momentum equations, along with the continuity equation, to obtain the desired solution. It was found that convergence to a satisfactory solution occurred in only a few iterations for a two-dimensional trajectory case and in less than 10 for a three-dimensional trajectory case.

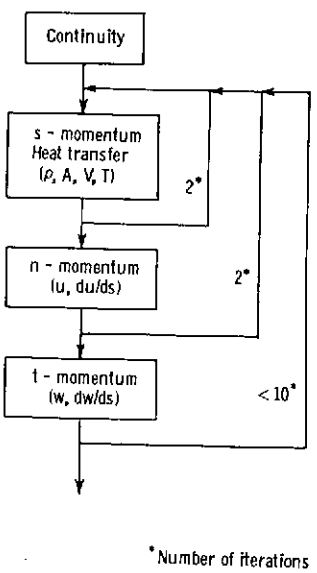

Figure 10.- Flow chart illustrating iteration of governing equations at a specific location on jet trajectory.

Incremental values of x, y, and z are obtained from the final value of trajectory slope and from the assigned value for Δs. These increments are added to the coordinates of the previous location on the trajectory to obtain new x,y,z trajectory coordinates. This procedure is repeated at each incremental "step" along the trajectory to provide a solution for the trajectory and cross-sectional area of the jet, as well as the jet flow properties of mass, velocity, momentum, and temperature. The theoretical results presented herein were obtained with a constant incremental step size of $0.01d_j$.

EXAMINATION OF THEORETICAL RESULTS

The purpose of this section is to discuss some of the limitations of the theory developed in the previous section and to demonstrate its versatility for handling a variety of injection situations. In order to establish the authenticity of the present theoretical method for estimating jet flow properties, its predictions are compared with estimates from other analytical models as well as with experimental data acquired from a number of studies. The last portion of the section presents a theoretical example of a jet with a three-dimensional trajectory.

Two-Dimensional Trajectory

Experimental trajectory data obtained from different investigations of air jets are presented in figures 11 and 12 and show the two-dimensional paths of the turbulent jet for a range of injection velocities and orientations. These data were obtained from hot-wire measurements and, thus, represent the path that is traced by the maximum velocity in the jet flow. The measurements show that an increase in injection velocity or angle α_i results in farther penetration of the jet into the free-stream flow. Theoretical trajectories were calculated with the same injection conditions as the experimental data and are in good agreement with the measured trajectories throughout the range of injection velocities and orientations.

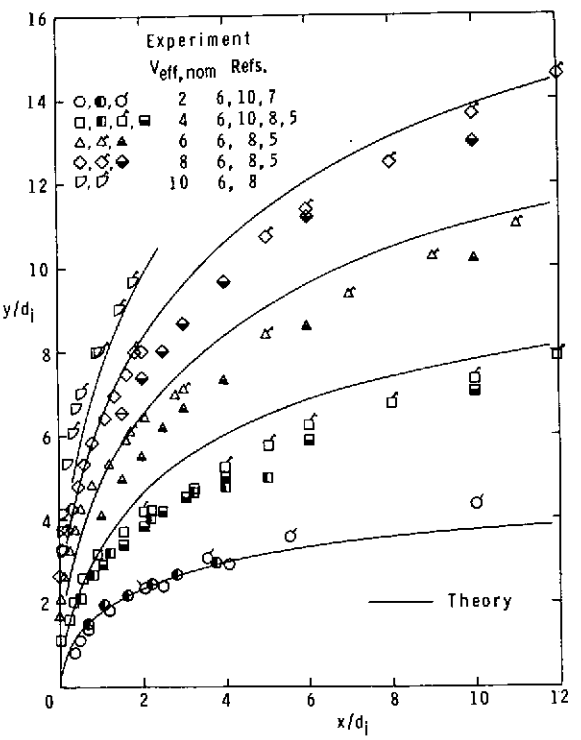

Figure 11.- Experimental and theoretical trajectories of an air jet having a range of injection velocities. $\alpha_i = 90^\circ$; $\beta_i = 0^\circ$.

Experimental trajectories are presented in figures 13, 14, and 15 for a water injection process where the jet is injected perpendicular $(\alpha_i = 90^\circ)$ to the direction of

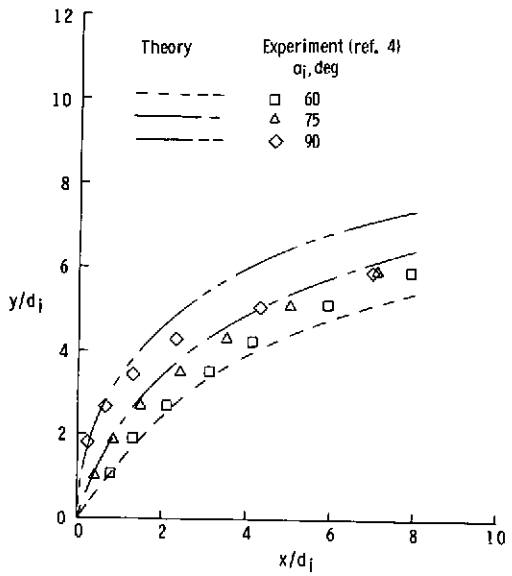

(a) $V_{eff} = 4.05$.

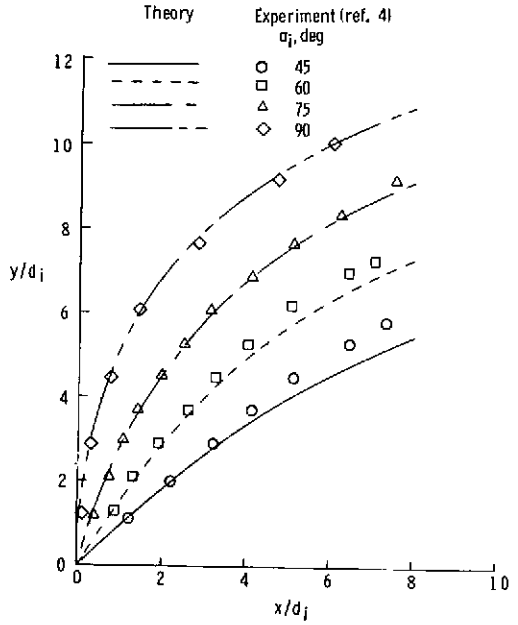

(b) $V_{eff} = 6.32$.

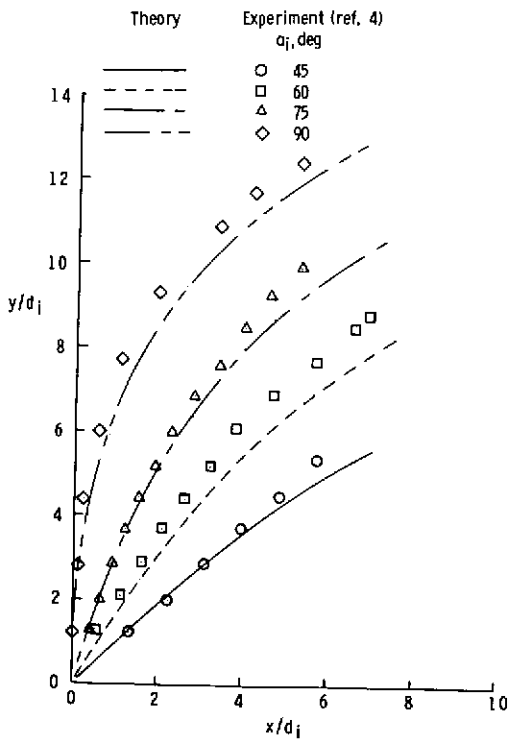

(c) $V_{eff} = 8.32$.

Figure 12.- Effect of injection angle on experimental and theoretical trajectories of an air jet. $\beta_i = 0^o$.

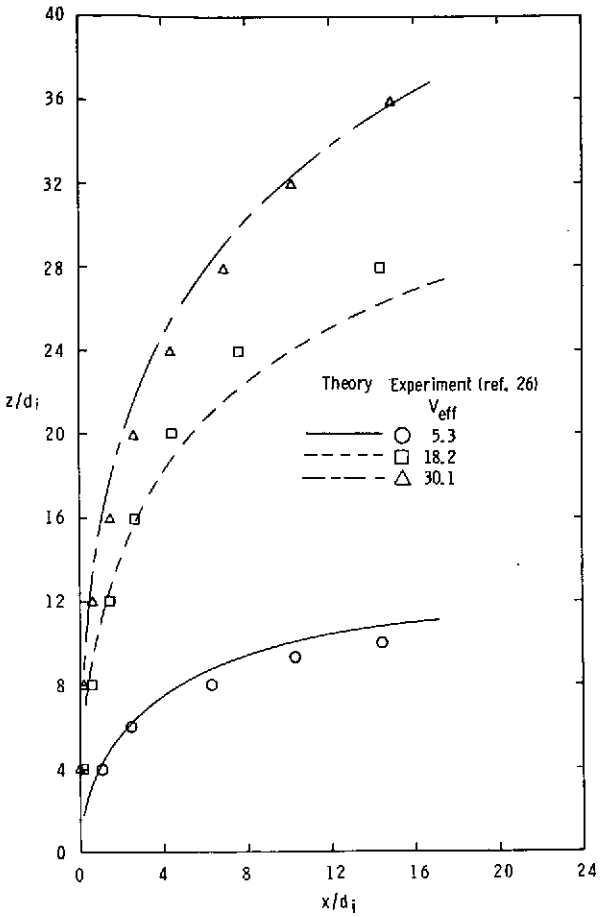

Figure 13.- Experimental and theoretical trajectories for lateral injection process. ΔT_j = -1.1 K; α_j = 90°; β_j = 90°.

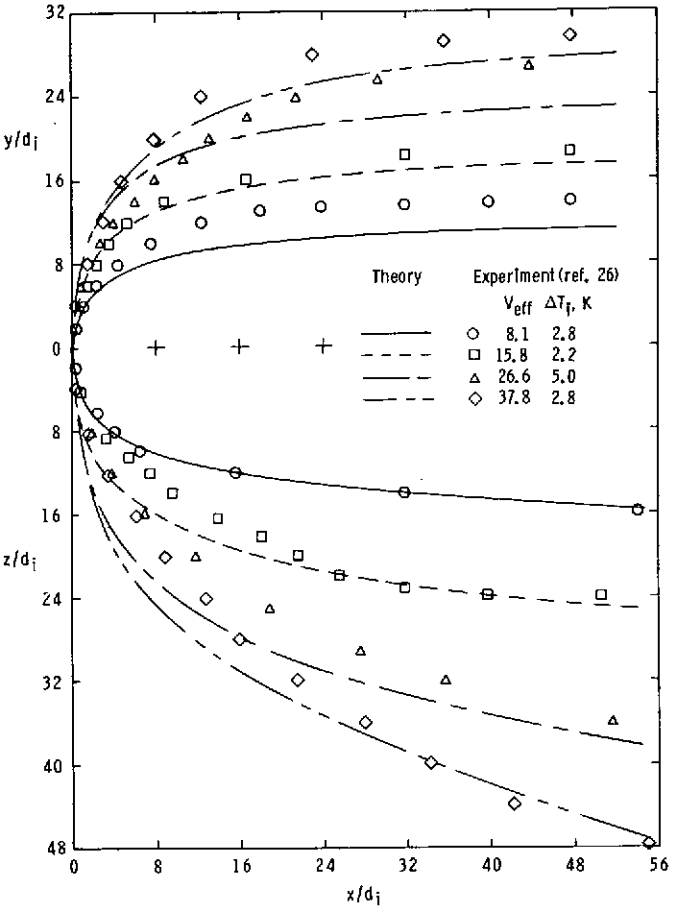

Figure 14.- Experimental and theoretical trajectories for oblique injection process. α_j = 90°; β_j = 50°.

flow in a water channel. The trajectories were measured from photographs of the jet injecting laterally $(\beta_j = 90^\circ)$, obliquely $(\beta_j = 50^\circ)$, and vertically $(\beta_j = 0^\circ)$ into the main stream, and, thus, they represent the path of the approximate center line of the jet flow. The information for the oblique injection process (fig. 14) is presented as the projection of the trajectories onto the vertical (X-Y) and horizontal (X-Z) planes. The effect of increasing injection velocity on the trajectories of these water jets is the same as that observed for the air jets; that is, the jet penetrates farther into the main stream with increase in injection velocity.

Theoretical trajectories calculated with the same injection conditions as the experimental data adequately represent the trend of increasing jet penetration with injection velocity and are in good agreement with the measured trajectories for the lateral and oblique injection processes (figs. 13 and 14, respectively). However, the present theory (represented in fig. 15 as a solid line) does not predict the amount of penetration experienced by the jet injected vertically. The reason for this discrepancy is that the experi-

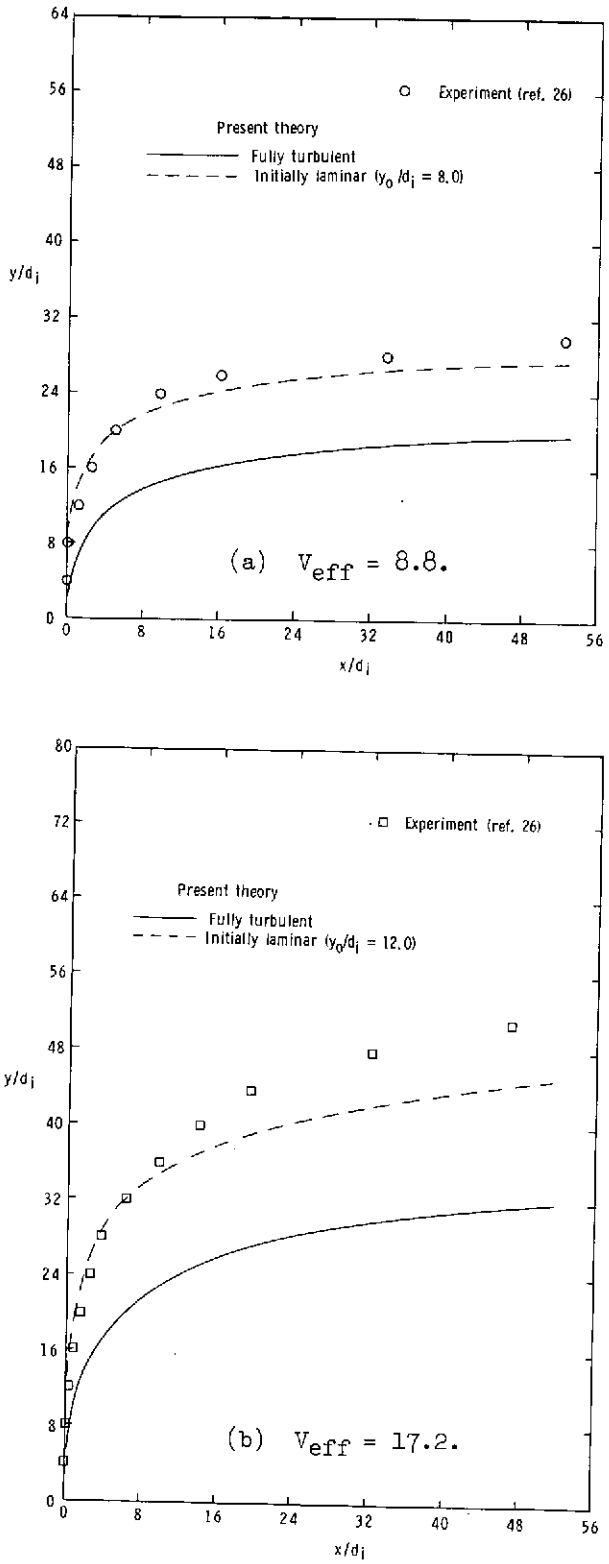

Figure 15.- Experimental and theoretical trajectories for the vertical injection process. ΔT_i = -1.67 K; experimental trajectories are for jets with initially laminar flow; $\alpha_i = 90^o$; $\beta_i = 0^o$.

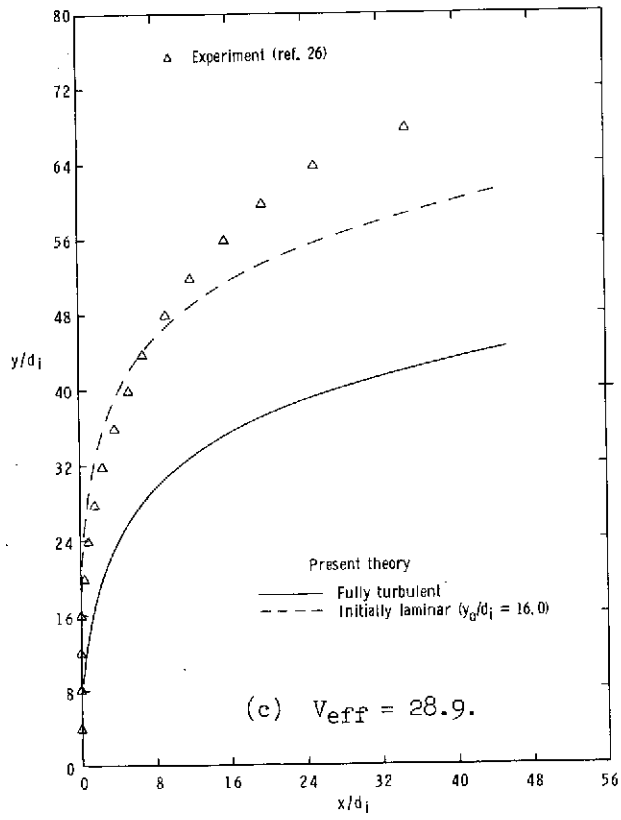

Figure 15.- Concluded.

mental results of figures 13 and 14 were obtained for completely turbulent jet flows, whereas the data in figure 15 were acquired for jet flows that are laminar at the injection point. It is recalled, of course, that the theory was developed by assuming fully turbulent flow. In order to estimate the trajectories for this mixed-flow situation, the present theory was adjusted to account for the initial laminar portion of the jet flow. This adjustment was accomplished by assuming that the jet begins its turbulent growth at a point y_o/d_i specified in the photographs in reference 26. Since the location and extent of the transition region in the flow are functions of injection conditions (e.g., $N_{Re,di}$), as well as free-stream conditions (e.g., V_{eff}), it is expected that the values of y_o/d_i will change accordingly. The appropriate values of y_o/d_i used to modify the theory are shown in figure 15 and the resulting calculations represented by the dashed lines.

Theoretical trajectories calculated with the present theory are compared with theoretical and experimental results of other researchers in figures 16 to 19. The analytical methods of Abramovich (ref. 10), Schetz and Billig (ref. 15), and Reilly (ref. 16) provide jet trajectories which are comparable to those of the present theory for the injection conditions presented (figs. 16 and 17). It is recalled that the theories of references 10, 15,

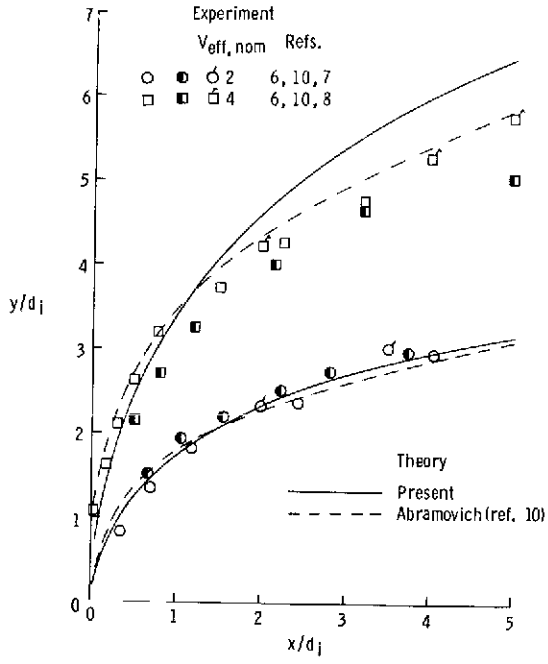

Figure 16.- Comparison of theoretical trajectories estimated by present theory and by Abramovich (ref. 10). $\alpha_i = 90°$; $\beta_i = 0°$.

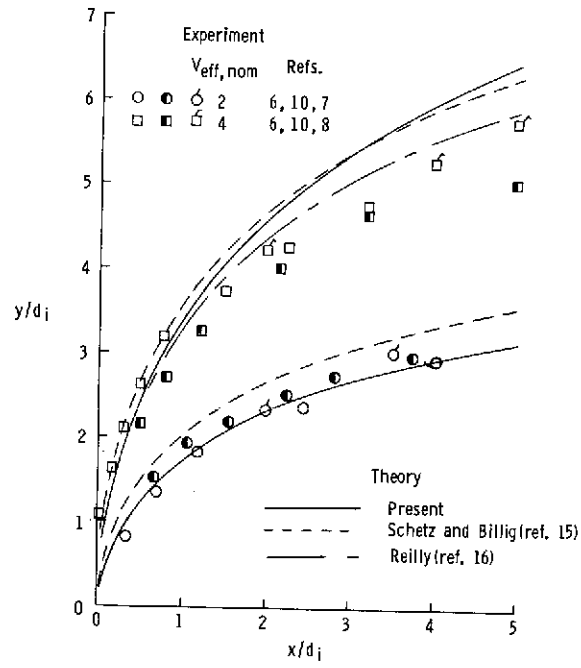

Figure 17.- Comparison of theoretical trajectories estimated by present theory with those of Schetz and Billig (ref. 15) and Reilly (ref. 16). $\alpha_i = 90°$; $\beta_i = 0°$.

and 16 assumed the growth of the jet cross-sectional area along the trajectory by using an empirical expression (fig. 6) based on experimental data for $s/d_j \leq 10$. As a consequence, the trajectories predicted by these theories agree quite well with experimental data in the vicinity of the injection point. Care must be exercised in using these theories to estimate jet trajectories and flow properties at large s/d_j values.

One of the best theoretical methods prior to the present is that of Hirst (ref. 21), who attempts to account for the complex flow processes that take place as the flow evolves from a momentum jet near the injection point to a buoyant plume at large distances downstream. His results are compared with the present theory in figures 18 and 19 for a range of injection velocities and angles. As noted, the present theory is in better agreement with the bulk of experimental data for all of the injection conditions. Since Hirst assumed a Gaussian type of velocity distribution in the jet, his theory is applicable only in the region where the jet flow has become fully developed. This explains why his theoretical trajectories do not originate at the injection point. The experimental data obtained by Gordier (ref. 2) are shown in figure 18 because Hirst compared his theory with these data in reference 21. Gordier's data, however, indicate greater penetration by the jet than is seen for the other data. Ramsey (ref. 7) suggested that this discrepancy was probably due to injection into a cross flow with a very thick boundary layer. This trend is shown later.

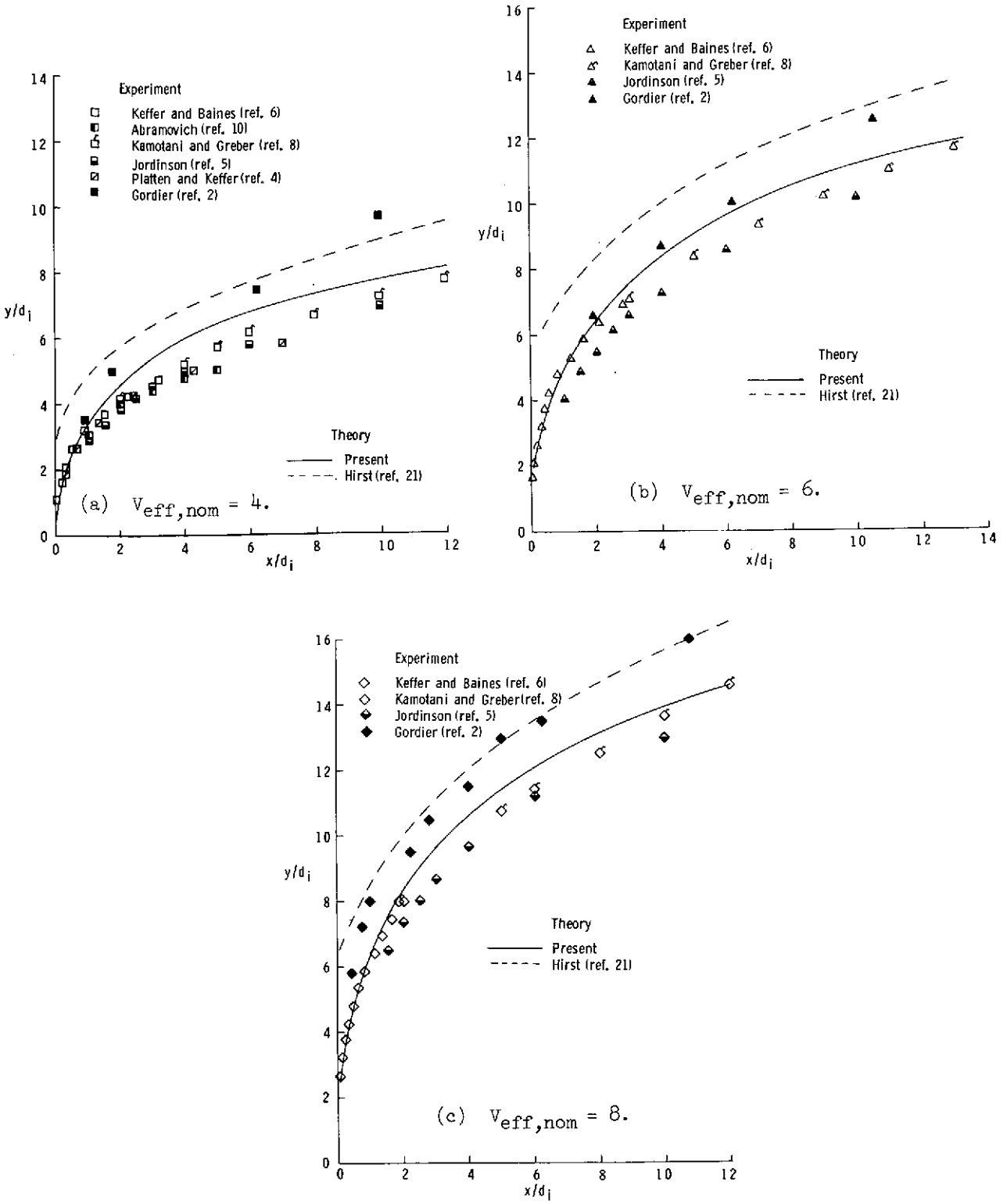

Figure 18.- Comparison of theoretical trajectories estimated by present theory with those of Hirst for normal injection. $\alpha_i = 90^\circ$; $\beta_i = 0^\circ$.

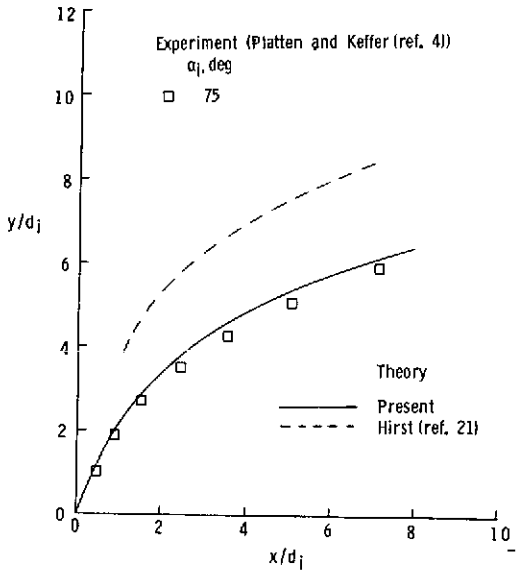

(a) $V_{eff} = 4.05$.

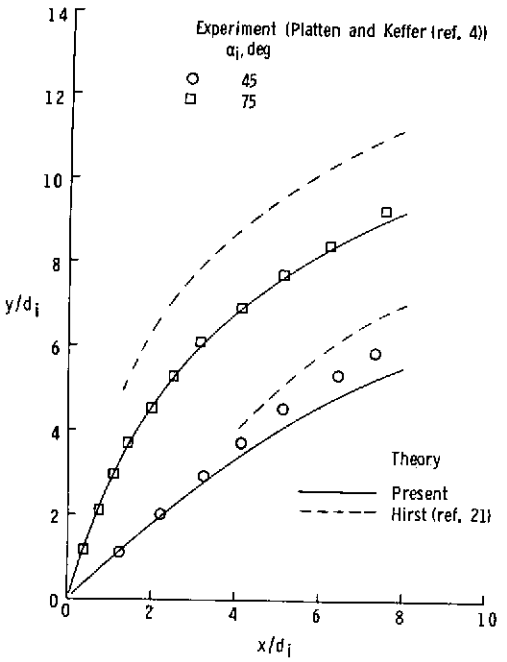

(b) $V_{eff} = 6.32$.

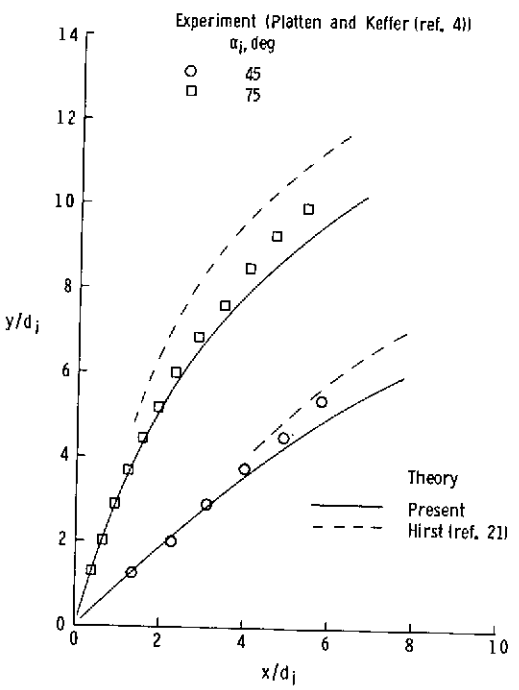

(c) $V_{eff} = 8.32$.

Figure 19.- Comparison of theoretical trajectories estimated by present theory with those of Hirst. $\alpha_i = 90^\circ$; $\beta_i = 0^\circ$.

Jet Flow Properties

Examples of some of the theoretical flow properties obtained in the process of solving the governing conservation equations are presented in figures 20 to 25. Experimental jet areas are shown in figure 20 normalized by the jet area at the injection point and plotted as functions of s/d_i. These measurements indicate that the cross-sectional area of the jet continually increases as the jet proceeds along the trajectory. The data points acquired from Kamotani and Gerber's work (ref. 8) were obtained by measuring the area encompassed by a contour of jet velocity where the velocity excess had decreased to 10 percent of the maximum excess with respect to the free-stream velocity component tangent to the jet flow. It is noted that Keffer and Baines (ref. 6) also defined the edge of the jet flow in this fashion. Experimental areas for $V_{eff,nom} = 30$ were obtained from the photographic information in reference 22 by assuming the cross-sectional shape to be a 5:1 ellipse and by measuring the minor axis. The data in figure 20 also indicate that an increase in injection velocity results in larger rates of area growth with s/d_i.

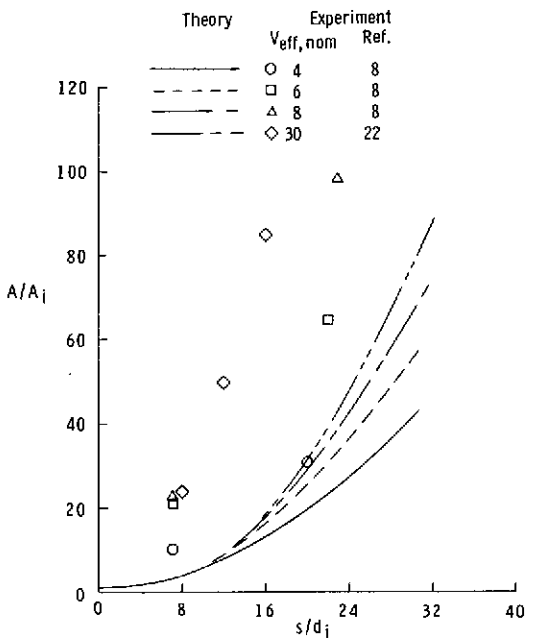

Figure 20.- Variation of jet cross-sectional area with distance along trajectory for a range of injection velocities. $\alpha_i = 90^\circ$. (Values from ref. 8 are measurements of the area bounded by a contour of jet velocity).

Theoretical areas are shown for comparison and predict the same trends as the experimental areas; however, the theory underestimates the magnitude of the area growth experienced by the jet for the range of injection velocities shown. It should be mentioned that these theoretical estimates of jet area are very sensitive to the amount of entrainment, small increases in entrainment resulting in large increases in the cross-sectional areas. It will be shown shortly from mass-flow arguments that the entrainment model used in the theory could be improved, which would result in better agreement between the theory and the experiment in figure 20.

As the area occupied by the jet fluid grows with increase in distance along the trajectory, the jet velocity correspondingly decays; this is illustrated in figure 21 where the jet velocity is nondimensionalized by the injection velocity and where the V_∞/V_i values for the various injection conditions are depicted by the arrows. The experimental data that are shown are measurements of the maximum jet velocity for $V_{eff,nom} = 4$, and 8

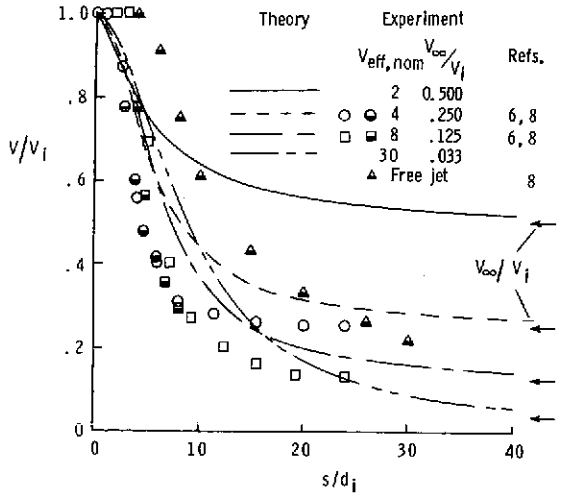

Figure 21.- Effect of injection velocity on jet velocity decay with increase in distance along trajectory. $\alpha_i = 90°$.

and for a free jet. These data indicate that the trend for velocity decay is similar for all injection velocities.

For all the cases, there is a short distance (potential core) where the maximum jet velocity remains equal to the injection velocity. Increase in s/d_i beyond this point results in continued decreases in jet velocity which eventually approaches the free-stream velocity value V_∞/V_i (note arrows in fig. 21). Increasing injection velocity increases the potential core length, a maximum value being obtained for the free jet (ref. 8), and decreases the value of V_∞/V_i that the jet velocity must approach, $V_\infty/V_i = 0$ for the free jet. The combination of these experimental trends helps in comprehending the theoretical velocity decay curves presented in the figure for a range of injection velocities. Comparing the theoretical velocities with the experimental data for $V_{eff,nom} = 4$ and 8 shows that the theory predicts V/V_i values that are greater than the experimental values and that approach V_∞/V_i at a slower rate. The fact that the mathematical model estimates average jet velocities explains why the theory predicts a decrease in velocity immediately after injection compared with the existence of a potential core demonstrated by the maximum velocity measurements.

The effects of increased injection velocity on velocity decay, which were discussed in connection with figure 21, are put into perspective in figure 22 by plotting the velocity as a velocity deficit, where the difference between the jet and free-stream velocity is divided by the difference at the injection point. Presenting the results in this fashion causes the velocity deficit to approach zero as $V \to V_\infty$. As noted, an increase in $V_{eff,nom}$ results in a corresponding increase in experimental velocity deficit at a given distance on the trajectory. This trend also applies essentially to the theoretical velocity deficit variations. Keffer and Baines (ref. 6) observed that velocity deficit showed a universality (i.e., independent of V_{eff}) when plotted against the distance from the virtual source of the jet flow.

The variation of theoretical mass flow in the jet with distance along the trajectory is shown in figure 23 for a range of injection velocities. As would be expected from our consideration of mass conservation in figure 3, the mass flow in the jet increases with increased distance along the trajectory, the higher mass flows occurring for the lower injection velocities. This increase in mass flow with increase in s/d_i is demonstrated

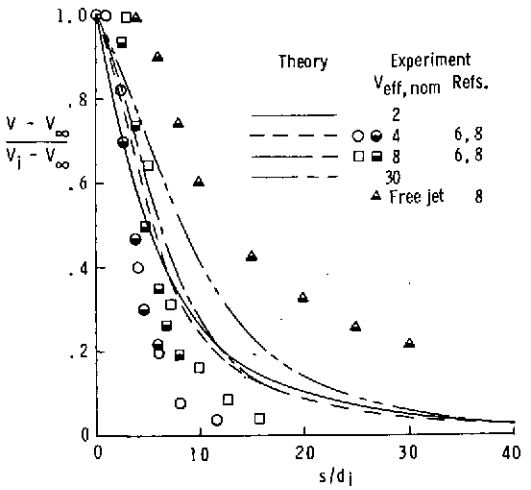

Figure 22.- Variation of jet velocity deficit with distance along trajectory for range of injection velocities. $\alpha_i = 90^\circ$.

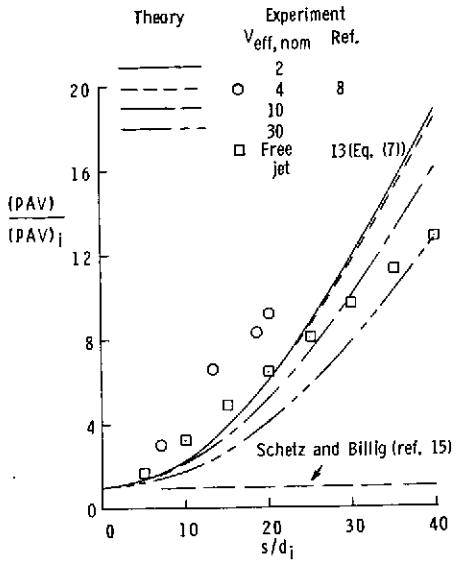

Figure 23.- Variation of mass flow in jet with distance along trajectory for range of injection velocities. $\alpha_i = 90^\circ$.

by experimental data (ref. 8) for $V_{eff,nom} = 4$, although the measured values indicate higher mass flows in the jet than are predicted by the theory. A further indication that the theoretical mass flows should be greater than they are is provided by the measurements of mass flow in a free jet. (See ref. 13.) The fact that these mass flows are less than the experimental values for the jet with $V_{eff,nom} = 4$ supports the premise that the entrainment rate for a jet in a cross flow should be greater than that for a free jet. At certain values of s/d_j the disturbing situation exists that the theory predicts mass flows that are less than the free-jet values. Improvements in the entrainment model used in the current analytical effort will provide improved estimates of the jet mass flow and consequently will yield more realistic cross-sectional area and velocity decay results than were observed in the last few figures. In the study by Schetz and Billig (ref. 15), the mass flow was assumed to remain constant at the initial value. Their assumption is represented by the horizontal dashed line in the figure and becomes more realistic nearer the injection point.

The variation of theoretical jet momentum with distance along the trajectory is shown in figure 24 for a range of injection velocities. The jet momentum, normalized by the value at the injection point, is seen to decrease immediately after injection and reach a point on the trajectory where it attains a minimum value, after which it increases for the remainder of the trajectory. This trend occurs for a jet injected normal to a free-stream flow because the component of momentum in the y-direction initially decreases along the trajectory faster than the component in the x-direction increases. For this

situation $\alpha_i = 90^\circ$ and the y- and s-momenta are identical at the injection point, so that the natural decrease of y-momentum with increase in s/d_i results in a decrease in s-momentum during the initial phase of the injection process. As the jet axis becomes parallel to the free-stream direction, the y-momentum of the jet approaches zero and the x- and s-momenta become synonymous.

The continual decrease of the y-momentum along the trajectory of a jet injected normal to a cross flow is illustrated in figure 25, where experimental data of Kamotani and Greber (ref. 8) are presented for several injection velocities. As you would expect, the y-momentum is largest (at a given s/d_i location) for the jet with the highest injection velocity. These trends of y-momentum with increase in s/d_i and V_{eff} are also reflected by the theoretical results of the present study. Abramovich (ref. 10) assumed in his analytical development that the component of jet momentum perpendicular to the free-stream direction (y-momentum) remains constant along the trajectory. The fallacy of this assumption is particularly obvious at large s/d_i distances.

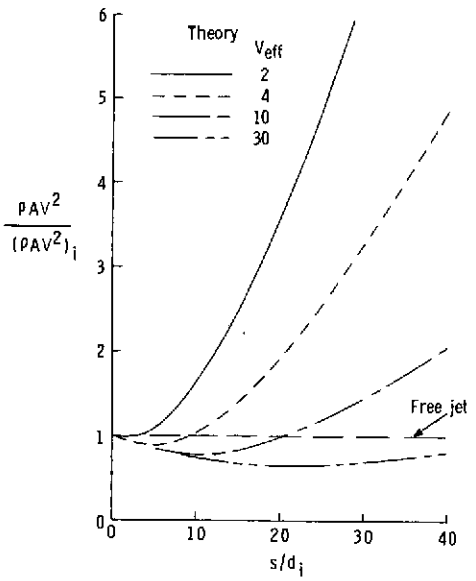

Figure 24.- Variation of theoretical jet momentum with distance along trajectory for range of injection velocities. $\alpha_i = 90^\circ$; $\beta_i = 0^\circ$.

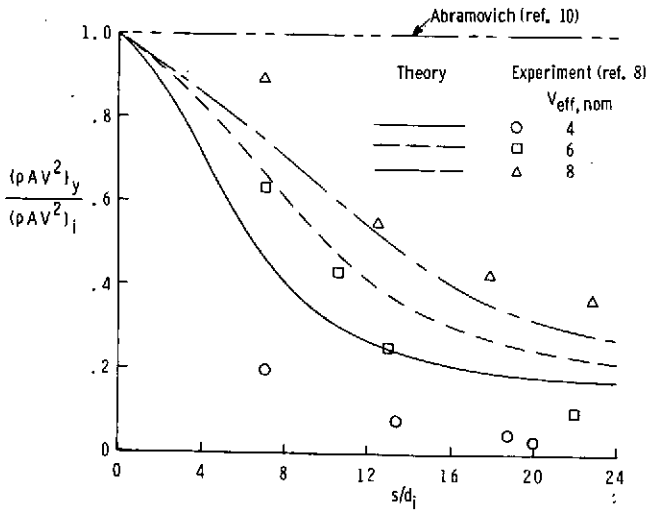

Figure 25.- Effect of injection velocity on the change of jet y-momentum with distance along trajectory. $\alpha_i = 90^\circ$; $\beta_i = 0^\circ$.

Free-Stream Nonuniformities

One advantage of the present theory is its flexibility for investigating parameters which affect the trajectory and flow properties of the injected jet. Not the least important of these parameters are the free-stream velocity and temperature fields into which the jet is injected. Up until now the free-stream velocity and temperature have been assumed

constant, but some of the effects resulting from relaxing these assumptions are demonstrated in figures 26 to 29. A water injection process is used for this demonstration.

For the purpose of this illustration, the jet is assumed to inject vertically into a free-stream flow which has a boundary-layer type of velocity distribution in the y-direction (fig. 26(a)). A Karman-Pohlhausen velocity function is described from the injection surface to the boundary-layer edge, which is taken to be $8d_j$. At larger values of y/d_j the velocity is assumed to be constant having the same value as V_∞ used for the uniform free-stream velocity case shown in figure 26(b). Figure 27 shows that injection into the nonuniform free-stream velocity field results in farther penetration by the jet into the cross flow than injection into the free stream with the uniform velocity field. Coincident with this, the jet velocity decay is essentially unaffected, whereas the jet cross-sectional area and momentum are less at any given distance along the trajectory. It was noted that the effect of free-stream velocity nonuniformity on jet trajectory diminished with increase in injection velocity.

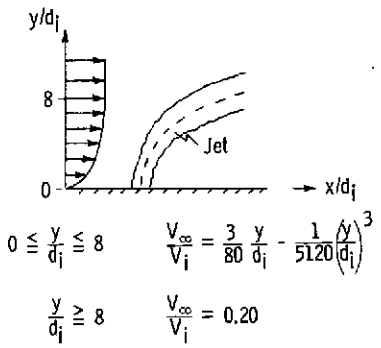

(a) Nonuniform free-stream velocity.

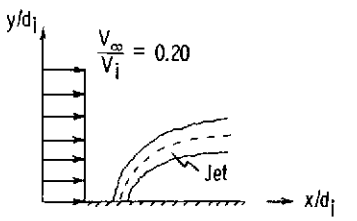

(b) Uniform free-stream velocity.

Figure 26.- Uniformity of free-stream velocity field. $\alpha_j = 90^\circ$; $\beta_j = 0^\circ$.

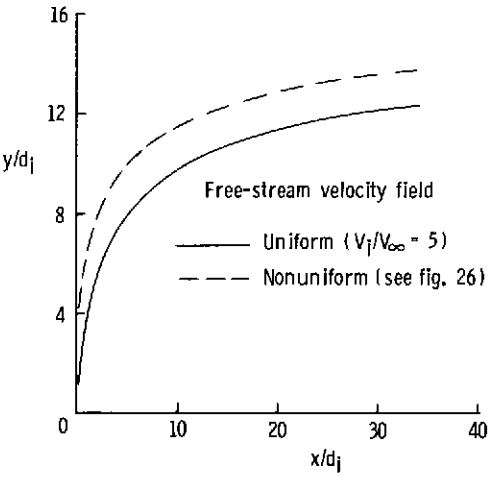

Figure 27.- Effect of free-stream velocity nonuniformity on theoretical trajectory. $\alpha_j = 90^\circ$; $\beta_j = 0^\circ$.

The linear temperature gradient shown in figure 28 is used to demonstrate the effect of injecting a heated jet vertically into a free-stream flow having constant velocity and nonuniform temperature fields. The free-stream temperature at the injection surface (295.4 K) is equivalent to the value used for the uniform free-stream temperature

case. Injecting a jet with initial temperatures of (295.4 K) and (306.5 K) into a free-stream flow having a uniform temperature results in the trajectory and temperature curves shown in figure 29. The combination of the jet flow having a very large Froude number and experiencing a rapid heat loss results in no change in the trajectory. This result agrees with the experimental observations made by Kamotani and Greber (ref. 8). As noted in the figure, the temperature for the heated jet decreases along the trajectory until it reaches the free-stream value $\left(T_\infty/T_j\right)$. Injection of the heated jet into the free-stream flow with a temperature gradient results in a trajectory similar to that obtained by injecting the heated jet into the uniform temperature field. There is a definite difference, however, in the temperature curves resulting for these two injection conditions, where the nonuniform T_∞ situation results in higher jet temperatures because of the larger values of T_∞ that the jet flow "sees" as it penetrates into the cross flow. Heat is initially lost from this jet flow until a point is reached on the trajectory where a heat gain is experienced.

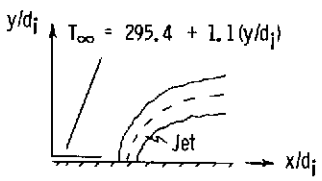

(a) Nonuniform free-stream temperature.

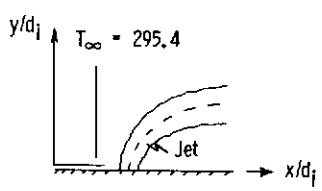

(b) Uniform free-stream temperature.

Figure 28.- Uniformity of free-stream temperature field. $\alpha_i = 90^\circ$; $\beta_i = 0^\circ$.

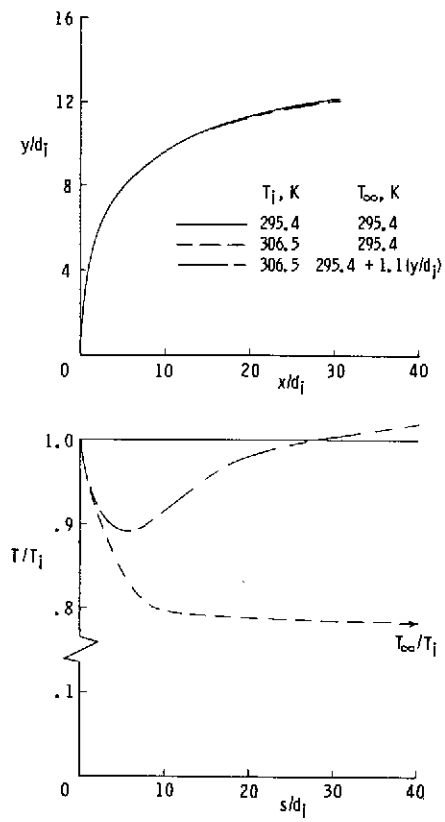

Figure 29.- Effect of free-stream temperature nonuniformity on theoretical jet trajectory and temperature. $V_{eff} = 5$; $\alpha_i = 90^\circ$; $\beta_i = 0^\circ$.

Three-Dimensional Trajectory

Up until now all the theoretical trajectories that have been presented are, by definition, two dimensional; that is, they lie in a single plane. Figures 30 and 31 are presented to illustrate a three-dimensional path that results for a water injection process where a jet is injected normal $(\alpha_i = 90^o)$ to the mainstream and rotated 45^o away from the vertical. An injection situation similar to this was observed in figure 14, where the theoretical trajectories are actually two dimensional because the Froude number of the jet flow is so large; or in other words, the buoyancy force is small compared to the momentum forces. In order to obtain a three-dimensional trajectory, particularly near the injection point, the Froude number of the jet flow must be small.

For the purpose of this demonstration, the heat transfer from the jet is ignored so that the jet density is assumed constant along the trajectory. Solutions for the governing conservation equations were obtained for $N_{Fr,i} \to \infty$ $(\text{i.e.,}\ \rho_i = \rho_\infty)$ and for $N_{Fr,i} = 10$; the projections of the resulting trajectories on the X-Y and X-Z planes are presented in figure 30. For $N_{Fr,i} \to \infty$, the projections on the two planes are equivalent which occurs only when $\beta_i = 45^o$ and the trajectory is two dimensional. Allowing ρ_i to be less than ρ_∞ leads to the second set of projections, which shows that decreasing the Froude number increases the penetration of the jet into the cross flow. The fact that the effect is more pronounced on the X-Y projection than on the X-Z projection is an indication that the triad of unit vectors associated with the natural coordinate system is tracing out a three-dimensional path. In effect these unit vectors are "twisting" out of the plane where the two-dimensional trajectory obtained for $N_{Fr,i} \to \infty$ is located.

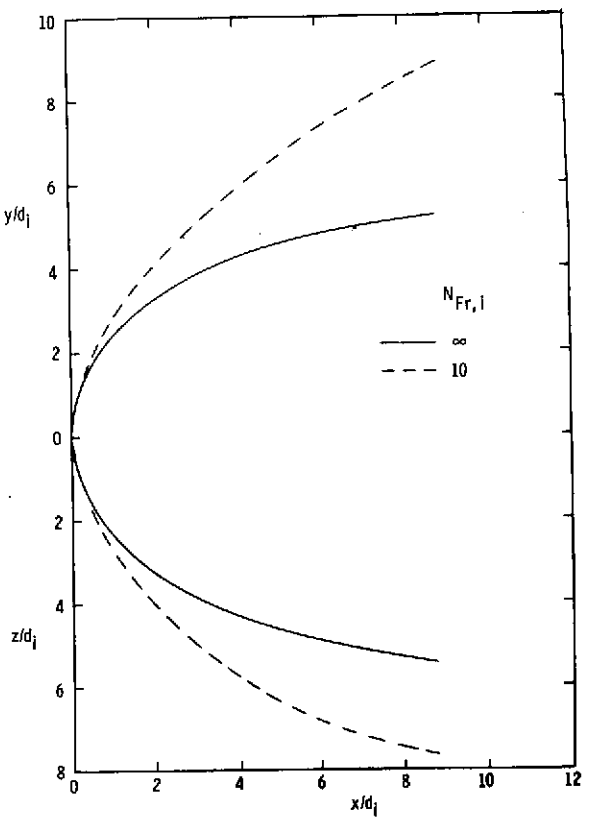

Figure 30.- Effect of Froude number on jet trajectory for $V_i/V_\infty = 4$. $\alpha_i = 90^o$; $\beta_i = 45^o$.

Further evidence that these numerical results are consistent can be obtained by examining the dependent variables of the governing equations (u and w) and their gradients. This information is presented in figure 31 where the injection conditions are identical to those used in figure 30, and the parameters in question are plotted as functions of distance along the trajectory. The solid curves represent the case where

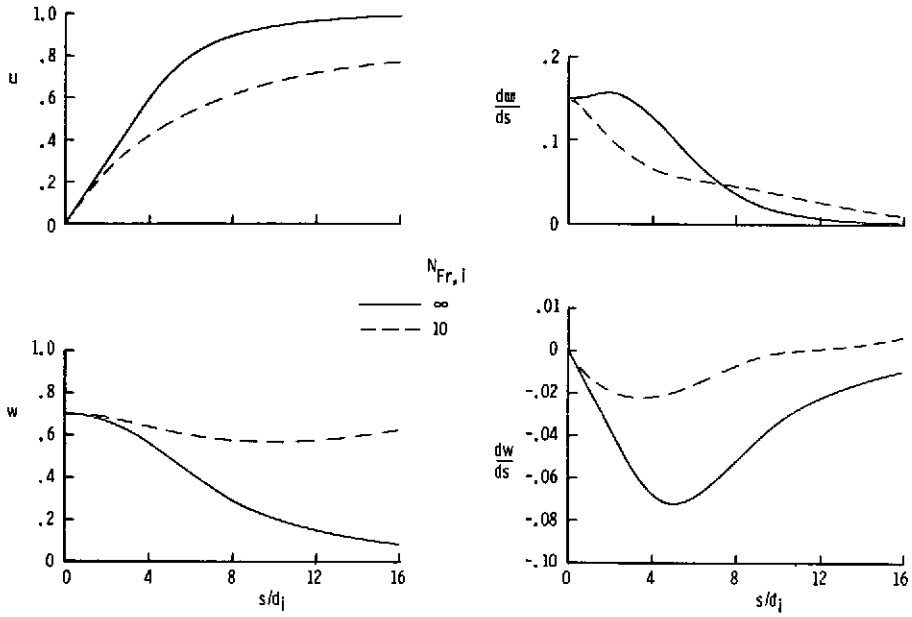

Figure 31.- Effect of Froude number on variation of jet trajectory parameters with distance along trajectory for $V_j/V_\infty = 4$. $\alpha_j = 90^\circ$; $\beta_j = 45^\circ$.

buoyancy force is zero $(N_{Fr,i} \to \infty)$ and are typical of the trends that result for injections with $0^\circ \leq \alpha_j \leq 90^\circ$ and $0^\circ \leq \beta_j \leq 90^\circ$. As noted, an increase in s/d_j results in a continual increase in u and a decrease in w, u and w approaching 1.0 and 0.0, respectively, for large s/d_j. These limits coincide with the jet velocity vector which becomes parallel to the free-stream velocity vector. In conjunction with these trends for u and w, du/ds and dw/ds are, respectively, positive and negative valued.

The dashed curves indicate what happens to the trajectory parameters when a sizable buoyancy force is considered. The fact that the values of u and w which result when $N_{Fr,i} = 10$ are, respectively, smaller and larger than the corresponding values when $N_{Fr,i} \to \infty$ is indicative of the increase in penetration experienced by the jet when the buoyancy force is added. An interesting aspect of this situation is seen in the variation of w with s/d_j, where w reaches a minimum value at some point on the trajectory and then begins to increase. This is the same as saying that β achieves a maximum value and then begins to decrease. The trend of w with s/d_j is reflected in the dw/ds curve, where dw/ds changes from its usual negative sign to a positive value. This result is important because it signifies that buoyancy force is becoming dominant over the other forces acting on the jet flow. It is intuitively obvious that for the situation where buoyancy is the driving force, the jet path will tend toward the vertical so that w will be increasing with increase in s/d_j and dw/ds will be greater than zero. This can be shown explicitly by letting $V_\infty = u = du/ds = 0$ in the n-momentum equation presented in appendix B (eq. (B9)) and by solving the resulting expression for dw/ds.

It is not possible to substantiate the trends discussed herein with results from other studies, since no experimental data exists for a jet with a three-dimensional trajectory. In the theoretical development of reference 21, it was stated that the governing equations could apply to a jet following a three-dimensional path; however, no calculations of a three-dimensional trajectory were presented to support that claim.

CONCLUDING REMARKS

An investigation has been conducted to develop a theoretical method which accounts for the pertinent fluid mechanic and heat-transfer aspects of heated turbulent jets discharging into a cross flow. The injection process was assumed to be incompressible, where the jet flow injects into a cross flow of semi-infinite extent having a spatially dependent velocity field.

A theoretical model of the jet was developed by using an integral method, which accounts for natural fluid mechanisms such as turbulence, entrainment, buoyancy, and heat transfer. Solving the governing conservation equations yielded predictions of jet trajectory and area growth that agreed well with experimental results for air and water injection processes having a wide range of injection conditions. Because the present investigation obtained the jet cross-sectional area in the process of solving the governing equations (unlike previous studies), the present theory allowed a prediction for various jet flow properties, such as velocity and momentum, to be obtained and provided better estimates for the jet trajectory.

Realistic estimates of temperature in the jet fluid were obtained by accounting for heat losses in the jet flow due to forced convection and to entrainment of free-stream fluid into the jet. Forced convection was seen to be the dominant heat-transfer mechanism during the early stages of the jet injection process, whereas the effects of entrainment became dominant as the jet penetrated further into the free-stream flow.

The versatility of the theory was demonstrated by observing the effects of a jet injected into free-stream flows with either a nonuniform velocity field or a nonuniform temperature field. Theoretical results were also shown to illustrate a truly three-dimensional jet trajectory which was calculated by considering the injection Froude number to be small.

Langley Research Center,
National Aeronautics and Space Administration,
Hampton, Va., September 25, 1973.

APPENDIX A

SPACE CURVE INFORMATION

This appendix provides additional information about the natural coordinate system used in the analytical study and presents the expressions necessary to transform the momentum equations in the text to the form used in the numerical solution.

Space Curves

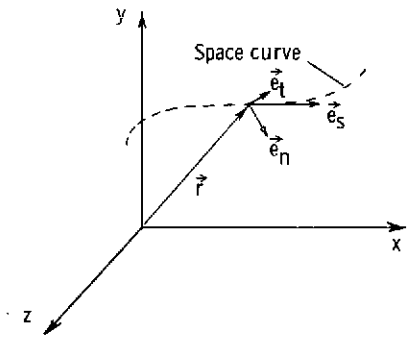

(a) Natural coordinate system.

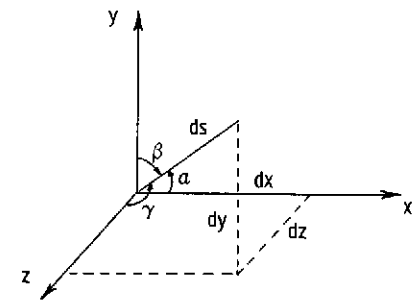

(b) Direction cosines of $\vec{e}_s$.

Figure 32.- Illustration of the natural coordinate system and the direction cosines of the unit vector $\vec{e}_s$.

The theoretical development utilizes a natural coordinate system that is associated with the path of the jet flow which consists of a moving triad of unit vectors $\vec{e}_s$, $\vec{e}_n$, and $\vec{e}_t$. This coordinate system is illustrated in figure 32(a) where $\vec{r}$ is the position vector from the origin to a point on the curve and is given by

$$\vec{r} = x\vec{e}_x + y\vec{e}_y + z\vec{e}_z \tag{A1}$$

The derivative of a position vector is shown by Hildebrand (ref. 27) to be a unit vector tangent to the curve and pointing in the direction of increasing arc length as follows:

$$\vec{e}_s = \frac{d\vec{r}}{ds} = \frac{dx}{ds}\vec{e}_x + \frac{dy}{ds}\vec{e}_y + \frac{dz}{ds}\vec{e}_z \tag{A2}$$

It is noted that $d\vec{r}/d\tilde{t}$ is the velocity vector associated with a point moving with speed $ds/d\tilde{t}$ along the curve. Thus,

$$\vec{V} = \frac{ds}{d\tilde{t}}\frac{d\vec{r}}{ds} = V\vec{e}_s \tag{A3}$$

Since $\vec{e}_s$ is a unit vector, it follows that

$$\left(\frac{dx}{ds}\right)^2 + \left(\frac{dy}{ds}\right)^2 + \left(\frac{dz}{ds}\right)^2 = 1 \tag{A4}$$

The derivative of $\vec{e}_s$ with respect to s has a direction perpendicular to the curve and is written as

$$\frac{d\vec{e}_s}{ds} = \frac{d^2x}{ds^2}\vec{e}_x + \frac{d^2y}{ds^2}\vec{e}_y + \frac{d^2z}{ds^2}\vec{e}_z \tag{A5}$$

where the length of this vector is the curvature of the curve. Defining the radius of curvature R as the reciprocal of the curvature and $\vec{e}_n$ as the unit vector in a direction normal to $\vec{e}_s$ gives

$$\frac{d\vec{e}_s}{ds} = \frac{1}{R}\vec{e}_n \tag{A6}$$

so that

$$\frac{1}{R} = \left[\left(\frac{d^2x}{ds^2}\right)^2 + \left(\frac{d^2y}{ds^2}\right)^2 + \left(\frac{d^2z}{ds^2}\right)^2\right]^{1/2} \tag{A7}$$

A moving, rotating triad of mutually orthogonal unit vectors is completely described by the addition of the third unit vector $\vec{e}_t$ which by definition is

$$\vec{e}_t = \vec{e}_s \times \vec{e}_n \tag{A8}$$

It is noted that for a plane curve, $\vec{e}_s$ and $\vec{e}_n$ lie in the plane of the curve, whereas $\vec{e}_t$ is a constant unit vector perpendicular to that plane. The trajectory resulting from the vertical injection process is an example of this situation. Differentiating equation (A8) leads to

$$\frac{d\vec{e}_t}{ds} = -\tau_o\vec{e}_n \tag{A9}$$

where the scalar τ_o is the torsion of the curve, the negative sign implying that τ_o is positive when the vector triad rotates in a right-handed sense about $\vec{e}_s$ as it progresses along the curve.

In order to find $d\vec{e}_n/ds$, write $\vec{e}_n = \vec{e}_t \times \vec{e}_s$ and differentiate to get

$$\frac{d\vec{e}_n}{ds} = \tau_o\vec{e}_t - \frac{1}{R}\vec{e}_s \tag{A10}$$

Equations (A6), (A9), and (A10) are known as the Frenet-Serret formulas. Taking the dot product of $\vec{e}_t$ with $d\vec{e}_n/ds$ leads to an expression for torsion which can be written in determinant form as

APPENDIX A

$$\tau_o = R^2 \begin{vmatrix} dx/ds & dy/ds & dz/ds \\ d^2x/ds^2 & d^2y/ds^2 & d^2z/ds^2 \\ d^3x/ds^3 & d^3y/ds^3 & d^3z/ds^3 \end{vmatrix} \tag{A11}$$

The dot products that are required in the governing momentum equations can now be found. For example, $\vec{e}_x \cdot \vec{e}_n$ and $\vec{e}_y \cdot \vec{e}_n$ are needed in the n-momentum expression (eq. (26)). Using equations (A5) and (A6) yields

$$\vec{e}_n = R \frac{d^2\vec{r}}{ds^2} \tag{A12}$$

so that

$$\vec{e}_x \cdot \vec{e}_n = R \frac{d^2x}{ds^2} \tag{A13}$$

and

$$\vec{e}_y \cdot \vec{e}_n = R \frac{d^2y}{ds^2} \tag{A14}$$

A similar procedure is used to get the dot products needed for the s-momentum expression:

$$\vec{e}_x \cdot \vec{e}_s = \frac{dx}{ds} \tag{A15}$$

and

$$\vec{e}_y \cdot \vec{e}_s = \frac{dy}{ds} \tag{A16}$$

The process for obtaining the dot products for the t-momentum expression (eq. (43)) is more involved because of the use of $\vec{e}_t$. The equation for $\vec{e}_t$ is found from equation (A10) to be

$$\vec{e}_t = \frac{1}{\tau_o} \frac{d}{ds} \left(R \frac{d^2\vec{r}}{ds^2} \right) + \frac{1}{R\tau_o} \frac{d\vec{r}}{ds} \tag{A17}$$

Taking the dot product of $\vec{e}_x$ and $\vec{e}_y$, respectively, with this expression and using the distributive law for dot products leads to

$$\vec{e}_x \cdot \vec{e}_t = \frac{1}{\tau_o}\frac{dR}{ds}\frac{d^2x}{ds^2} + \frac{R}{\tau_o}\frac{d^3x}{ds^3} + \frac{1}{R\tau_o}\frac{dx}{ds} \tag{A18}$$

and

$$\vec{e}_y \cdot \vec{e}_t = \frac{1}{\tau_o}\frac{dR}{ds}\frac{d^2y}{ds^2} + \frac{R}{\tau_o}\frac{d^3y}{ds^3} + \frac{1}{R\tau_o}\frac{dy}{ds} \tag{A19}$$

Direction Cosines

It was mentioned in the section "Theoretical Development" that the procedure for solving the governing equations (6), (27), (38), and (44) simultaneously was simplified by using the direction cosines of the unit vector $\vec{e}_s$ as the dependent variables. The angles $\vec{e}_s$ makes with the X-, Y-, and Z-axes are shown in figure 32(b) and are defined as

$$\cos\alpha = \frac{dx}{ds} \qquad \cos\beta = \frac{dy}{ds} \qquad \cos\gamma = \frac{dz}{ds} \tag{A20}$$

Equation (A4) represents the auxiliary equation for these direction cosines and is used to express the third direction cosine (dz/ds) in terms of the other two. Define

$$u = \frac{dx}{ds} \qquad w = \frac{dy}{ds} \tag{A21}$$

so that equation (A4) becomes

$$\frac{dz}{ds} = \left(1 - u^2 - w2\right)^{1/2} = \eta^{1/2} \tag{A22}$$

The derivatives of this expression are found to be

$$\frac{d^2z}{ds^2} = \frac{-u\dfrac{du}{ds} - w\dfrac{dw}{ds}}{\eta^{1/2}} = \frac{\Lambda}{\eta^{1/2}} \tag{A23}$$

and

APPENDIX A

$$\frac{d^3z}{ds^3} = \frac{\eta\left[-u\,\frac{d^2u}{ds^2} - \left(\frac{du}{ds}\right)^2 - w\,\frac{d^2w}{ds^2} - \left(\frac{dw}{ds}\right)^2\right] - \Lambda^2}{\eta^{3/2}} \tag{A24}$$

Expressions for R, dR/ds, τ_o

At this point it is desirable to obtain the expressions for R, dR/ds, and τ_o in terms of the direction cosines u and w. Equations (A21) and (A23) are substituted into equation (A7) to get the following expression for R:

$$\frac{1}{R} = \left[\left(\frac{du}{ds}\right)^2 + \left(\frac{dw}{ds}\right)^2 + \frac{\Lambda^2}{\eta}\right]^{1/2} \tag{A25}$$

The relation for dR/ds is obtained by differentiating R (eq. (A7)) and substituting the necessary auxiliary equations from equations (A21) to (A24) as follows:

$$-\frac{1}{R^3}\frac{dR}{ds} = \frac{du}{ds}\frac{d^2u}{ds^2} + \frac{dw}{ds}\frac{d^2w}{ds^2} + \frac{\Lambda}{\eta^{1/2}}\left\{-\frac{1}{\eta^{1/2}}\left[u\,\frac{d^2u}{ds^2} + \left(\frac{du}{ds}\right)^2 + w\,\frac{d^2w}{ds^2} + \left(\frac{dw}{ds}\right)^2\right] - \frac{\Lambda^2}{\eta^{3/2}}\right\} \tag{A26}$$

The torsion of the curve is obtained after some manipulation by expanding the determinant in equation (A11) and by substituting the auxiliary equations as follows:

$$\begin{aligned}\frac{\tau_o}{R^2} = &-\left(u\,\frac{dw}{ds} - w\,\frac{du}{ds}\right)\left\{\frac{1}{\eta^{1/2}}\left[u\,\frac{d^2u}{ds^2} + \left(\frac{du}{ds}\right)^2 + w\,\frac{d^2w}{ds^2} + \left(\frac{dw}{ds}\right)^2\right] + \frac{\Lambda^2}{\eta^{3/2}}\right\} \\ &+ \left(-\frac{\Lambda}{\eta^{1/2}}u + \eta^{1/2}\frac{du}{ds}\right)\frac{d^2w}{ds^2} + \left(\frac{\Lambda}{\eta^{1/2}}w - \eta^{1/2}\frac{dw}{ds}\right)\frac{d^2u}{ds^2}\end{aligned} \tag{A27}$$

Thus, equations (A25) to (A27) represent R, dR/ds, and τ_o as functions of u and w and their derivatives for the general case of a three-dimensional curve. It is interesting to note the forms these equations take when the trajectory is two dimensional, such as for a vertical injection process $(\gamma = 90^o)$. For this situation, the auxiliary equation (A22) becomes

$$u^2 + w^2 = 1 \qquad (\eta = 0) \tag{A28}$$

so that

$$\Lambda = u \frac{du}{ds} + w \frac{dw}{ds} = 0 \tag{A29}$$

Using these relations in equation (A25) leads to

$$\frac{1}{R} = \frac{1}{w} \frac{du}{ds} \tag{A30}$$

Likewise,

$$-\frac{1}{R^3} \frac{dR}{ds} = \frac{du}{ds} \frac{d^2u}{ds^2} + \frac{dw}{ds} \frac{d^2w}{ds^2} \tag{A31}$$

and $\tau_o = 0$. Torsion would be expected to equal zero from equation (A9) since the trajectory is a plane curve which implies that $\vec{e}_t$ is a constant vector (parallel to the Z-axis).

APPENDIX B

NONDIMENSIONAL CONSERVATION EQUATIONS

The purpose of this appendix is to nondimensionalize the governing conservation equations and to make several observations concerning their numerical solution. In addition, special forms of the governing equations are examined and the t-momentum equation is shown to be an identity for the vertical injection situation.

s-Momentum

The direction cosine expressions from appendix A are substituted into equation (38) and the resulting expression is divided by $\frac{(\rho AV^2)_i}{d_i}$ to get the nondimensionalized s-momentum equation as follows:

$$\frac{1}{(\rho AV^2)_i}\frac{d(\rho AV^2)}{d\bar{s}} = \frac{1}{2}\left(\frac{A}{A_i}\right)d_i\frac{g(\rho_\infty - \rho)w}{q_i} + \frac{1}{2}\left(\frac{A}{A_i}\right)\left(\frac{q_\infty}{q_i}\right)\left[\bar{R}\frac{d\bar{R}}{d\bar{s}}\left(\frac{du}{d\bar{s}}\right)^2 + \bar{R}^2\frac{du}{d\bar{s}}\frac{d^2u}{d\bar{s}^2}\right] + J\left(\frac{V_\infty}{V_i}u\right) \tag{B1}$$

where the barred symbols indicate division by d_i. The expression

$$E = J\frac{(\rho AV)_i}{d_i} \tag{B2}$$

was also used in the process of obtaining equation (B1).

As was mentioned in the section "Solution Procedure," equation (B1) is solved at point $j+1$ for the jet momentum which is estimated by using a backward finite difference to approximate the rate of change of ρAV^2 with s. This gives

$$\left.\frac{d(\rho AV^2)}{d\bar{s}}\right|_{j+1} = \frac{(\rho AV^2)_{j+1} - (\rho AV^2)_j}{\Delta\bar{s}} \tag{B3}$$

which can be substituted into equation (B1). The momentum $(\rho AV^2)_{j+1}/(\rho AV^2)_i$ is calculated by using values for the various parameters in equation (B1) evaluated at j as a first estimate, and then using $j+1$ values after the first iteration. The jet momentum is then used in conjunction with $(\rho AV)_{j+1}$ to provide values for V_{j+1} and, hence, A_{j+1}.

At this point in the numerical solution the heat loss from the jet control volume is accounted for. It should be recalled (see eq. (45)) that the mass of fluid in the control

volume must be specified before and after entrainment takes place in order to calculate the effect of entrainment on jet temperature. The total mass in the control volume after entrainment is given by

$$m_{j+1} = m_j + m_e \tag{B4}$$

where the entrained mass m_e is found to be

$$m_e = \frac{(\Delta s)^2 E}{V_e} \tag{B5}$$

The velocity of entrainment V_e is taken to be an average velocity in the control volume; equation (6) is used in conjunction with the E^* function presented in figure 3 to specify E.

n-Momentum

The expressions for the direction cosines (appendix A) are substituted into equation (27) and the resulting equation is divided by ρAV^2. The ratio of mass flow in the jet to the initial jet mass flow is written as

$$K = \frac{\rho AV}{(\rho AV)_i} \tag{B6}$$

and is used to get the nondomensional n-momentum equation as follows:

$$\frac{1}{\overline{R}} = G_1 \overline{R} \frac{dw}{d\overline{s}} + G_2 \overline{R}^2 \left(\frac{du}{d\overline{s}}\right)^2 + G_3 \overline{R} \frac{du}{d\overline{s}} \tag{B7}$$

where

$$\overline{R} = \frac{R}{d_i}$$

$$G_1 = \frac{d_i}{2}\left(\frac{\rho}{\rho_i}\right)\left(\frac{A}{A_i}\right)^2 \frac{g(\rho_\infty - \rho)}{K^2 q_i}$$

$$G_2 = \frac{2\overline{h}}{\pi K^2} C_{D,n}\left(\frac{q_\infty}{q_i}\right)\left(\frac{\rho}{\rho_i}\right)\left(\frac{A}{A_i}\right)$$

$$G_3 = \frac{J}{K^2}\left(\frac{V_\infty}{V_i}\right)\left(\frac{\rho}{\rho_i}\right)\left(\frac{A}{A_i}\right)$$

APPENDIX B

In order to put equation (B7) into the form used in the numerical solution, the expression for R must be considered (eq. (A25)). Examining the vertical injection case results in a cubic equation in du/ds after equations (A25), (A28), (A29), and (A30) are substituted into equation (B7). It is noted that two roots of the cubic equation are zero if the buoyancy term is neglected. This type of trivial solution can be avoided by dividing du/ds out of equation (A25) to get

$$\frac{1}{\bar{R}} = \frac{du}{d\bar{s}}\left[1 + \left(\frac{dw}{du}\right)^2 + \frac{\left(u + w\,\frac{dw}{du}\right)^2}{1 - u^2 - w^2}\right]^{1/2} = A_1\,\frac{du}{d\bar{s}} \tag{B8}$$

which is substituted into equation (B7) to get the following transformed n-momentum equation:

$$\frac{du}{d\bar{s}} = \frac{G_1}{A_1^{\,2}}\,\frac{dw}{du} + \frac{G_3}{A_1^{\,3}} + \frac{G_4}{A_1^{\,2}} \tag{B9}$$

This equation is used to calculate $(du/ds)_{j+1}$, with u_{j+1}, w_{j+1}, $(dw/du)_{j+1}$, G_1, G_2, and G_3 being known. Appropriate values of u are then obtained by utilizing

(1) A backward finite-difference scheme at the first step away from the injection point (i.e., $\bar{s} = \Delta\bar{s}$)

$$u_{j+1} = u_j + \Delta\bar{s}\left(\frac{du}{d\bar{s}}\right)_{j+1} \tag{B10}$$

(2) A central finite-difference scheme to get u_{j+2} at points on the remainder of the trajectory (i.e., $\bar{s} > \Delta\bar{s}$)

$$u_{j+2} = u_j + 2(\Delta\bar{s})\left(\frac{du}{d\bar{s}}\right)_{j+1} \tag{B11}$$

For the vertical or lateral injection situations, the auxiliary relation (eq. (A22)) can be used to obtain a value of w_{j+2} corresponding to the value of u_{j+2} in equation (B11), while its derivative

$$u\,\frac{du}{ds} + w\,\frac{dw}{ds} = 0 \tag{B12}$$

can be used to obtain a value of $(dw/ds)_{j+1}$ and, hence, $(dw/du)_{j+1}$. These parameters are used to iterate through the governing equations to obtain a solution for the two-dimensional trajectory. For the more general injection cases, the t-momentum equation is required to provide information on w and its derivatives.

t-Momentum

The direction cosine expressions from appendix A are substituted into equation (44) and the resulting relation is divided by d_i/q_i to obtain the nondimensional t-momentum equation as follows:

$$F_1\bar{\tau}_o\frac{d\bar{R}}{d\bar{s}} + F_2\bar{\tau}_o\frac{d^2w}{d\bar{s}^2} + F_3\bar{\tau}_o + F_4\left(\frac{d\bar{R}}{d\bar{s}}\right)^2 + F_5\left(\frac{d^2u}{d\bar{s}^2}\right)^2 + F_6 + F_7\frac{d\bar{R}}{d\bar{s}}\frac{d^2u}{d\bar{s}^2}$$
$$+ F_8\frac{d^2u}{d\bar{s}^2} + F_9\frac{d\bar{R}}{d\bar{s}} + F_{10}\bar{\tau}_o\frac{d\bar{R}}{d\bar{s}} + F_{11}\bar{\tau}_o\frac{d^2u}{d\bar{s}^2} + F_{12}\bar{\tau}_o = 0 \qquad \text{(B13)}$$

where $\bar{\tau}_o = \tau_o d_i$ and

$$F_1 = \frac{gA}{d_i q_i}(\rho_\infty - \rho)\frac{dw}{d\bar{s}} \qquad F_2 = \frac{gA\bar{R}}{d_i q_i}(\rho_\infty - \rho)$$

$$F_3 = \frac{gAw}{d_i q_i \bar{R}}(\rho_\infty - \rho) \qquad F_4 = \frac{\bar{h}}{5}C_{D,t}\left(\frac{q_\infty}{q_i}\right)\left(\frac{du}{d\bar{s}}\right)^2$$

$$F_5 = \frac{\bar{h}}{5}C_{D,t}\left(\frac{q_\infty}{q_i}\right)\bar{R}^2 \qquad F_6 = \frac{\bar{h}}{5}C_{D,t}\left(\frac{q_\infty}{q_i}\right)\frac{u^2}{\bar{R}^2}$$

$$F_7 = \frac{2\bar{h}}{5}C_{D,t}\left(\frac{q_\infty}{q_i}\right)\bar{R}\frac{du}{d\bar{s}} \qquad F_8 = \frac{2\bar{h}}{5}C_{D,t}\left(\frac{q_\infty}{q_i}\right)u$$

$$F_9 = \frac{2\bar{h}}{5}C_{D,t}\left(\frac{q_\infty}{q_i}\right)\frac{u}{\bar{R}}\frac{du}{d\bar{s}} \qquad F_{10} = \frac{\pi}{2}J\left(\frac{V_\infty}{V_i}\right)\frac{du}{d\bar{s}}$$

$$F_{11} = \frac{\pi}{2}J\left(\frac{V_\infty}{V_i}\right)\bar{R} \qquad F_{12} = \frac{\pi}{2}J\left(\frac{V_\infty}{V_i}\right)\frac{u}{\bar{R}}$$

APPENDIX B

It has been seen in equations (A26) and (A27) that dR/ds and τ_o are functions of d^2w/ds^2 and d^2u/ds^2 plus lower order terms. The approach used here is to define d^2u/ds^2 by using a finite difference approximation after a solution has been obtained from equation (B9). The problem then becomes one of getting dR/ds and τ_o in terms of d^2w/ds^2. Thus, from equation (A26),

$$\frac{dR}{ds} = B_1 + B_2\left(\frac{d^2w}{ds^2}\right) \tag{B14}$$

and from equation (A27),

$$\tau_o = B_3 + B_4\left(\frac{d^2w}{ds^2}\right) \tag{B15}$$

where the B coefficients are functions of u, w, du/ds, dw/ds, and d^2u/ds^2. When these relations are substituted into the t-momentum equation (eq. (B13)), a quadratic expression in d^2w/ds^2 results as follows:

$$B_5\left(\frac{d^2w}{ds^2}\right)^2 + B_6\frac{d^2w}{ds^2} + B_7 = 0 \tag{B16}$$

The coefficients are calculated from information obtained from the n-momentum equation, and a solution is acquired at point j+1 by approximating d^2w/ds^2 with a central finite difference. This results in a quadratic in w_{j+2}, which is solved to provide an update on w_{j+2}, $(dw/ds)_{j+1}$, and $(dw/du)_{j+1}$.

It is desirable to demonstrate that the t-momentum equation is an identity for the vertical injection situation where the trajectory is two dimensional and is confined to the X-Y plane. For this case, $\vec{e}_t$ is parallel to the Z-axis which implies that the dot products of this vector with $\vec{e}_x$ and $\vec{e}_y$ in equation (43) are zero; hence, the t-momentum equation is an identity. This fact can be shown in a more rigorous fashion by considering the expressions for $(\vec{e}_x \cdot \vec{e}_t)$ and $(\vec{e}_y \cdot \vec{e}_t)$ from equations (A18) and (A19). Substituting for direction cosines into these two equations gives

$$R\frac{d^2u}{ds^2} + \frac{dR}{ds}\frac{du}{ds} + \frac{u}{R} \stackrel{?}{=} 0 \tag{B17}$$

and

$$R\frac{d^2w}{ds^2} + \frac{dR}{ds}\frac{dw}{ds} + \frac{w}{R} \stackrel{?}{=} 0 \tag{B18}$$

where the desire is to prove that these relations are equal to zero for the vertical injection case. To do this it is necessary to use the auxiliary expressions that are presented in equation (A22), with $\eta = 0$, and in equation (B12). It is noted that equation (B17) can be written as

$$\frac{d}{ds}\left(R\frac{du}{ds}\right) + \frac{u}{R} \stackrel{?}{=} 0 \tag{B19}$$

The expression for R for a vertical injection case was shown in appendix A (equation (A30)) and is substituted into equation (B19) to get

$$u\frac{du}{ds} + w\frac{dw}{ds} \stackrel{?}{=} 0 \tag{B20}$$

which is definitely zero from equation (B12).

The procedure is similar for equation (B18) where

$$\frac{d}{ds}\left(R\frac{dw}{ds}\right) + \frac{w}{R} \stackrel{?}{=} 0 \tag{B21}$$

Equation (B12) is solved for dw/ds which, along with the relationship for R, is substituted into equation (B21) to obtain

$$-\frac{du}{ds} + \frac{du}{ds} \equiv 0 \tag{B22}$$

Thus, the dot products $\vec{e}_x \cdot \vec{e}_t$ and $\vec{e}_y \cdot \vec{e}_t$ are zero for the vertical injection situation; hence, the t-momentum equation (eq. (43)) is an identity. This fact was used as a check of the computer results to see that the numerical output from the t-momentum equation was correct.

REFERENCES

1. Margason, Richard J.; and Fearn, Richard: Jet-Wake Characteristics and Their Induced Aerodynamic Effects on V/STOL Aircraft in Transition Flight. Analysis of a Jet in a Subsonic Crosswind, NASA SP-218, 1969, pp. 1-18.

2. Gordier, Robert L.: Studies on Fluid Jets Discharging Normally Into Moving Liquid. Tech. Paper No. 28, Ser. B (Contract Nonr 710(26)), St. Anthony Falls Hydraulic Lab., Univ. of Minnesota, Aug. 1959.

3. Margason, Richard J.: The Path of a Jet Directed at Large Angles to a Subsonic Free Stream. NASA TN D-4919, 1968.

4. Platten, J. L.; and Keffer, J. F.: Deflected Turbulent Jet Flows. Trans. ASME, Ser. E: J. Appl. Mech., vol. 38, no. 4, Dec. 1971, pp. 756-758.

5. Jordinson, R.: Flow in a Jet Directed Normal to the Wind. R. & M. No. 3074, Brit. A.R.C., 1958.

6. Keffer, J. F.; and Baines, W. D.: The Round Turbulent Jet in a Cross-Wind. J. Fluid Mech., vol. 15, Pt. 4, Apr. 1963, pp. 481-497.

7. Ramsey, James Woodson: The Interaction of a Heated Air Jet With a Deflecting Flow. Ph. D. Thesis, Univ. of Minnesota, 1969.

8. Kamotani, Yasuhiro; and Greber, Isaac: Experiments on a Turbulent Jet in a Cross Flow. FTAS/TR-71-62 (NASA Grant NGR-36-027-008), Case Western Reserve Univ., June 1971. (Available as NASA CR-72893.) (Available in abbreviated form as AIAA Paper No. 72-149.)

9. Fricke, L. B.; Wooler, P. T.; and Ziegler, H.: A Wind Tunnel Investigation of Jets Exhausting Into a Crossflow. AFFDL-TR-70-154, Vols. I-IV, U.S. Air Force, Dec. 1970.

10. Abramovich, G. N.: The Theory of Turbulent Jets. M.I.T. Press, c.1963, pp. 541-553.

11. Keffer, James F.: The Physical Nature of the Subsonic Jet in a Cross-Stream. Analysis of a Jet in a Subsonic Crosswind, NASA SP-218, 1969, pp. 19-36.

12. Morton, B. R.: On a Momentum-Mass Flux Diagram for Turbulent Jets, Plumes, and Wakes. J. Fluid Mech., vol. 10, pt. 1, Feb. 1961, pp. 101-112.

13. Ricou, F. P.; and Spalding, D. B.: Measurements of Entrainment by Axisymmetrical Turbulent Jets. J. Fluid Mech., vol. 11, Pt. 1, Aug. 1961, pp. 21-32.

14. Thompson, Joe Floyd, Jr.: Two Approaches to the Three-Dimensional Jet-In-Cross-Wind Problem: A Vortex Lattice Model and a Numerical Solution of the Navier-Stokes Equations. Ph. D. Thesis, Georgia Inst. Technol., 1971.

15. Schetz, Joseph A.; and Billig, Frederick S.: Penetration of Gaseous Jets Injected Into a Supersonic Stream. J. Spacecraft & Rockets, vol. 3, no. 11, Nov. 1966, pp. 1658-1665.

16. Reilly, Richard Selmer: Investigation of the Deformation and Penetration of a Turbulent, Subsonic Jet Issuing Transversely Into a Uniform, Subsonic Main Stream. Ph. D. Diss., Univ. of Maryland, 1968.

17. Campbell, James F.; and Schetz, Joseph A.: Penetration and Mixing of Heated Jets in a Waterway With Application to the Thermal Pollution Problem. AIAA Paper No. 71-524, May 1971.

18. Wooler, P. T.; Burghart, G. H.; and Gallagher, J. T.: Pressure Distribution on a Rectangular Wing With a Jet Exhausting Normally Into an Airstream. J. Aircraft, vol. 4, no. 6, Nov.-Dec. 1967, pp. 537-543.

19. Hoult, David P.; Fay, James A.; and Forney, Larry J.: A Theory of Plume Rise Compared With Field Observations. J. Air Pollution Control Assoc., vol. 19, no. 8, Aug. 1969, pp. 585-590.

20. Hoult, D. P.; and Weil, J. C.: Turbulent Plume in a Laminar Cross Flow. Fluid Mech. Lab. Publ. No. 70-8, Massachusetts Inst. Technol., Oct. 1970.

21. Hirst, E. A.: Analysis of Round, Turbulent, Buoyant Jets Discharged to Flowing Stratified Ambients. ORNL-4685, U.S. At. Energy Comm., June 1971.

22. Campbell, James F.; and Schetz, Joseph A.: Flow Properties of Submerged Heated Effluents in a Waterway. AIAA J., vol. 11, no. 2, Feb. 1973, pp. 223-230.

23. Platten, J. L.; and Keffer, J. F.: Entrainment in Deflected Axisymmetric Jets at Various Angles to the Stream. UTME-TP-6808, Dept. Mech. Eng., Univ. of Toronto, June 1968.

24. Schlichting, Hermann (J. Kestin, transl.): Boundary-Layer Theory. Sixth ed., McGraw-Hill Book Co., Inc., 1968.

25. Eckert, E. R. G.; and Drake, Robert M., Jr.: Heat and Mass Transfer. McGraw-Hill Book Co., Inc., 1959, pp. 139, 239-243.

26. Campbell, J. F.; and Schetz, J. A.: Analysis of the Injection of a Heated, Turbulent Jet Into a Moving Mainstream, With Emphasis on a Thermal Discharge in a Waterway. VPI-E-72-24, Virginia Polytech. Inst. & State Univ., Dec. 1972. (Also available as Ph. D. Thesis by James F. Campbell.)

27. Hildebrand, Francis B.: Advanced Calculus for Applications. Prentice-Hall, Inc., c.1962, pp. 271-275.